tRNA synthetase activity is required for stress granule and P-body assembly

Max Baymiller,[1,2,3] Noah S. Helton,[1,2] Benjamin Dodd,[1,2] and Stephanie L. Moon[1,2]

[1]Department of Human Genetics, University of Michigan, Ann Arbor, Michigan 48109, USA; [2]Center for RNA Biomedicine, University of Michigan, Ann Arbor, Michigan 48109, USA; [3]Department of Molecular Biology and Biochemistry, Wesleyan University, Middletown, Connecticut 06459, USA

Translation elongation defects activate the integrated stress response (ISR), but whether and how ribosome stalls are cleared to enable mRNA release for ribonucleoprotein (RNP) granule assembly remain unclear. We show that blocking tRNA aminoacylation generates persistent uncollided ribosome stalls that inhibit stress granule and P-body assembly despite robust ISR activation. Collided ribosomes are rapidly cleared by ZNF598-dependent ribosome-associated quality control within 4 h, while uncollided stalls resist clearance and persist for >16 h. Puromycin releases persistent stalls and restores RNP granule formation. The block in stress granule assembly is generalizable across tRNA synthetase inhibitors and amino acid deprivation. Therefore, stress granules represent signal integrators reporting translation elongation status when initiation is suppressed. Our findings reveal that translation quality control pathways selectively clear collided ribosomes, establish that translation elongation stress uncouples RNP granule assembly from the ISR, and suggest that tolerating uncollided stalls may be adaptive for cotranslational processes essential for cellular function.

[*Keywords*: P-bodies; halofuginone; integrated stress response; ribosome-associated quality control; ribosome collisions; stress granules; tRNA synthetase; translation elongation]

Supplemental material is available for this article.

Received November 20, 2025; revised version accepted November 20, 2025.

Translation elongation stresses such as impaired tRNA metabolism, amino acid deprivation, UV, and other RNA-damaging agents inhibit translation and activate the integrated stress response (ISR) (Sundrud et al. 2009; Keller et al. 2012; Yan and Zaher 2021; Snieckute et al. 2022; Stoneley et al. 2022; Ryder et al. 2023; Boon et al. 2024; Misra et al. 2024; Sinha et al. 2024). The ISR suppresses translation initiation via eIF2α phosphorylation and reprograms gene expression for cellular adaptation to stress (Pakos-Zebrucka et al. 2016; Costa-Mattioli and Walter 2020). During the ISR, inhibition of translation initiation and ribosome runoff typically drives the assembly of nontranslating mRNAs and RNA binding proteins into biomolecular condensates called stress granules (SGs) and processing bodies (P-bodies or PBs) (Guillén-Boixet et al. 2020; Sanders et al. 2020; Yang et al. 2020; Baymiller and Moon 2023). These ribonucleoprotein (RNP) granules are implicated in many biological and disease contexts (Di Stefano et al. 2019; Dubinski et al. 2022; Song and Grabocka 2023; Burke et al. 2024; Pessina et al. 2025) and may contribute to cellular resilience to stress (Kedersha et al. 2013; Riback et al. 2017; Desroches Altamirano et al. 2024). While ribosome association with mRNAs (Moon et al. 2019, 2020; Baymiller and Moon 2023; Helton et al. 2025) and direct chemical inhibitors of ribosome translocation (Kedersha et al. 2000, 2005; Teixeira et al. 2005; Mazroui et al. 2006; Mollet et al. 2008; Khong and Parker 2018; Helton et al. 2025) inhibit RNP granule assembly, it is not clear whether or how mRNAs are released from stalled ribosomes during translation elongation stress to assemble into RNP granules. Addressing this issue requires interrogating whether and how ribosomes are cleared from mRNAs during elongation stress.

Stalled ribosomes can be removed from mRNA by the ribosome-associated quality control (RQC) pathway (Brandman et al. 2012; Juszkiewicz et al. 2020b) and ribosome rescue factors such as HBS1/PELO/ABCE1 (Doma and Parker 2006; Shoemaker et al. 2010) and GTPBP1/2 (Ishimura et al. 2014; Terrey et al. 2021). The RQC pathway recognizes and resolves collided ribosomes through sensing of the disome interface by the E3 ubiquitin ligase ZNF598 (Vind et al. 2020b; Wu et al. 2020). However, emerging evidence suggests that the RQC pathway can be overwhelmed (Stoneley et al. 2022) and cannot resolve

Corresponding author: smslmoon@umich.edu
Article published online ahead of print. Article and publication date are online at http://www.genesdev.org/cgi/doi/10.1101/gad.353535.125. Freely available online through the *Genes & Development* Open Access option.

all types of ribosome collisions (such as those caused by RNA–protein cross-links [Rahmanto et al. 2023; Zhao et al. 2023] or preinitiation complexes collided with ribosomes [Garshott et al. 2021]). The capacity of RQC pathways to clear different types of stalls, particularly uncollided versus collided stalled ribosomes, and the kinetics of stall resolution remain unclear.

Translation elongation defects activate multiple stress signaling pathways. The ISR is triggered by the eIF2α kinase GCN2 (general control nonderepressible 2) when elongation is impaired (Dever et al. 1992; Keller et al. 2012; Ishimura et al. 2016; Masson 2019; Misra et al. 2024). GCN2 can be activated by binding uncharged tRNAs (Wek et al. 1995; Dong et al. 2000; Yin et al. 2024) or by sensing stalled ribosomes through interactions with the ribosomal P-stalk (Harding et al. 2019; Inglis et al. 2019) or cofactor GCN1 at the collided ribosome interface (Wu et al. 2020; Pochopien et al. 2021; Yan and Zaher 2021). In these contexts, GCN2 mediates a negative feedback loop between translation elongation and initiation to reduce further ribosome stalling events and limit the production of protein fragments that can misfold and aggregate. In parallel, collided ribosomes and, to a lesser extent, uncollided stalled ribosomes trigger the ribotoxic stress response (RSR) (Vind et al. 2020b; Wu et al. 2020). The RSR is a less understood pathway that is activated when the kinase ZAKα senses stalled ribosomes and triggers p38 and JNK mitogen-activated protein kinase signaling pathways (Vind et al. 2020a,b; Wu et al. 2020; Sinha et al. 2024) and can result in inflammation, metabolic reprogramming, cell cycle arrest, and apoptosis (Vind et al. 2020a, 2024; Robinson et al. 2022; Snieckute et al. 2022; Sinha et al. 2024). Whether GCN2 and ZAKα activation during translation elongation stress results primarily from uncharged tRNAs or ribosome collisions and how the RQC pathway modulates their activation remain incompletely understood.

An important unresolved question is whether physiological translation elongation stresses generate ribosome stalls that can be cleared by translation quality control pathways. Determining whether and how ribosome stalls are sensed and resolved in physiological contexts will be important, as translation elongation defects and signaling pathways associated with ribosome stalling are observed in aging (Stein et al. 2022; Snieckute et al. 2023; Fu et al. 2024; Di Fraia et al. 2025) and neurological disease (Ishimura et al. 2014, 2016; Spaulding et al. 2021; Zuko et al. 2021) contexts. If ribosome stalls persist, mRNA retention in polysomes would be predicted to inhibit RNP granule assembly despite ISR activation. Alternatively, if ribosome stalls are efficiently cleared through RQC or ribosome rescue pathways, mRNAs would be released from polysomes and assemble into RNP granules. Distinguishing between these two possibilities requires direct measurement of ribosome stalling and collisions over time during physiologically relevant translation elongation stresses.

We addressed this question using tRNA synthetase inhibitors such as halofuginone that generate physiological ribosome stalls with A sites lacking aminoacylated tRNAs (Misra et al. 2021; Pitera et al. 2022). Halofuginone inhibits prolyl-tRNA charging by the glutamyl-prolyl tRNA synthetase EPRS1 and activates the ISR via GCN2 (Keller et al. 2012). In contrast to elongation inhibitors that directly bind the ribosome (e.g., cycloheximide and emetine) and do not inhibit aminoacylated tRNA from occupying the A site (Garreau de Loubresse et al. 2014; Wong et al. 2014; Wu et al. 2019; Enam et al. 2020; Eiler et al. 2024), many physiological contexts including tRNA synthetase inhibition result in ribosomes stalled with A sites that are not stably occupied, such as amino acid deprivation, truncated or damaged mRNAs, and mRNAs with suboptimal codons or internal poly(A) tracts (Shoemaker et al. 2010; Shao et al. 2016; You et al. 2017; Chandrasekaran et al. 2019; Tesina et al. 2020; Thomas et al. 2020; Yan and Zaher 2021; Aguilar Rangel et al. 2024). We thus performed time-resolved disome and polysome profiling, live- and fixed-cell fluorescence microscopy, and puromycin-mediated ribosome release experiments in wild-type and RQC-deficient *ZNF598* knockout cells to determine how ribosome stalls are processed during translation elongation stress.

We demonstrated that tRNA synthetase inhibition causes both collided and uncollided ribosome stalls. Although the ZNF598-dependent RQC pathway clears collided disomes within 4 h, uncollided stalls persist for >16 h without resolution. This selective ribosome clearance results in ISR activation but prevents the assembly of stress granules and P-bodies due to mRNA retention within stalled ribosomes. The peptidyl-tRNA mimic puromycin frees mRNAs from polysomes and rescues RNP granule assembly during tRNA synthetase inhibition. Persistent ribosome stalling is generalizable across tRNA synthetase inhibitors and amino acid deprivation, which also activate the ISR without inducing stress granules. These findings reveal fundamental limitations in translation surveillance and establish that elongation stress can uncouple RNP granule assembly from the ISR, with implications for aging, disease, and cellular stress adaptation.

Results

Inhibition of tRNA charging activates the integrated stress response and suppresses translation

We first assessed whether acute inhibition of tRNA synthetases activates the ISR. We performed experiments in U-2 OS cells, which are widely used to study ribosome-associated quality control, the ISR, and stress granules (Kedersha et al. 2005; Moon et al. 2019; Wu et al. 2020; Goldman et al. 2021; Snieckute et al. 2023; Helton et al. 2025) and have levels of major RQC/ribosome release factors similar to those of other commonly used cell lines and tissues (Supplemental Fig. S1). We treated U-2 OS cells with micromolar levels of halofuginone to rapidly and completely inhibit prolyl-tRNA charging for 1 h and assessed eIF2α phosphorylation and translation activity. We compared P-eIF2α levels upon halofuginone treatment versus arsenite and thapsigargin stresses, which activate the ISR via oxidative or endoplasmic reticulum stresses,

respectively. Consistent with prior studies (Sundrud et al. 2009; Keller et al. 2012; Kim et al. 2020b; Misra et al. 2021, 2024; Pitera et al. 2022), we observed that halofuginone significantly increased P-eIF2α levels (by 16.0-fold ± 1.5-fold), which was comparable with the levels of P-eIF2α induced by arsenite (21.0-fold ± 3.5-fold) and thapsigargin (13.8-fold ± 2.6-fold) (Fig. 1A). We then applied bioorthogonal noncanonical amino acid tagging (BONCAT) (Dieterich et al. 2006) to measure bulk protein synthesis during stress. We found that halofuginone caused an 84.0% ± 4.5% reduction in protein synthesis compared with unstressed cells as measured by BONCAT, which was comparable with the degree of translational suppression observed in arsenite and thapsigargin stresses (Fig. 1B). Therefore, inhibition of prolyl-tRNA charging activates the ISR and suppresses translation to a degree similar to canonical stressors.

tRNA synthetase activity is required for stress granule and P-body assembly

While inhibition of tRNA charging activates the ISR, the results of past studies suggest that translation elongation is also inhibited (Misra et al. 2021; Pitera et al. 2022). We next tested whether suppressing tRNA synthetase activity induced stress granule (SG) formation, as halofuginone robustly increased the levels of P-eIF2α. However, SG assembly is driven by the release of mRNAs from translation, which would require either ribosomes to run off of mRNAs or ribosome release through the RQC/RQT pathways (Kedersha et al. 2000, 2005; Mollet et al. 2008; Bengtson and Joazeiro 2010; Ishimura et al. 2014; Khong and Parker 2018; Moon et al. 2020; Helton et al. 2025). We treated U-2 OS cells expressing the SG marker protein GFP-G3BP1 (Burke et al. 2020) with halofuginone for 1 h and assessed SG formation. A key observation is that cells treated with halofuginone did not form SGs (Fig. 1C). In contrast, cells formed abundant SGs during treatment with canonical stressors arsenite and thapsigargin, which led to P-eIF2α levels similar to those seen in HF-treated cells (Fig. 1C). Furthermore, no SGs were detected in cells treated with halofuginone when visualizing other canonical SG markers including UBAP2L, PABPC1, and polyadenylated RNA (Fig. 1D). These results demonstrate that tRNA synthetase inhibitors do not cause SG formation despite activating the ISR.

To test whether inhibition of tRNA charging with halofuginone prevents SG assembly under conditions that cause SG formation, we cotreated cells with halofuginone and arsenite or thapsigargin. We observed that halofuginone cotreatment prevented SG formation by either arsenite or thapsigargin (Fig. 1E). Halofuginone cotreatment did not decrease P-eIF2α induction in response to arsenite (Supplemental Fig. S2A) or thapsigargin (Supplemental Fig. S2B), indicating that inhibition of SGs by halofuginone is not through reduced activation of the ISR. Thus, tRNA synthetase activity is required for SGs to form.

We next determined whether tRNA synthetase inhibition broadly impacts stress-induced cytoplasmic RNP granules by assessing the formation of processing bodies (P-bodies or PBs). P-bodies are enriched in RNA decay factors (e.g., DCP1A, EDC4, and XRN1), harbor nontranslating mRNAs, and interact with SGs during stress (Sheth and Parker 2003; Kedersha et al. 2005; Teixeira et al. 2005; Parker and Sheth 2007; Moon et al. 2019). We used immunofluorescence microscopy to detect the PB marker DCP1A in cells treated with halofuginone, arsenite, or thapsigargin. We found that halofuginone inhibited PB assembly (Fig. 1F). While 22.4% ± 2.0% of cells harbor PBs in the unstressed condition, 6.2% ± 1.3% of halofuginone-treated cells had PBs (Fig. 1F). In contrast, arsenite and thapsigargin induced PBs to 100.0% ± 0.0% and 95.7% ± 0.4%, respectively (Fig. 1F). Similar results were observed when immunofluorescence was used to detect additional canonical PB proteins—XRN1 and EDC4 (Fig. 1G). Therefore, tRNA synthetase inhibition does not induce PB assembly despite activating the ISR.

We next determined whether tRNA synthetase inhibition prevents the assembly of PBs in response to stress. We cotreated cells with halofuginone and arsenite or thapsigargin and measured PBs by staining for DCP1A. We observed that halofuginone significantly decreased the percentage of cells with PBs from 97.9% ± 1.2% to 52.9% ± 16.9% in arsenite stress and from 96.9% ± 0.5% to 7.5% ± 4.6% in thapsigargin stress (Fig. 1H). Together, these results suggest that tRNA charging is required for the assembly of stress-induced RNP granules.

Inhibition of tRNA charging blocks stress-induced mRNA release from polysomes

Inhibition of translation elongation by halofuginone causes ribosomes to accumulate on proline codons, at the 5′ end of coding sequences, and on mRNAs encoding proline-rich proteins (Misra et al. 2021; Pitera et al. 2022). Because we found that SG and PB assembly was blocked despite robust levels of P-eIF2α, we hypothesized that halofuginone would cause retention of mRNAs in polysomes, as ribosomes lack the charged prolyl-tRNA to elongate and allow ribosome runoff. To test this hypothesis, we used polysome profiling to measure mRNA association with ribosomes in lysates of cells treated with halofuginone or the canonical stressor thapsigargin. In support of our hypothesis, we found that unstressed cells exhibited robust polysomes with a high polysome:monosome ratio and that thapsigargin treatment caused polysomes to collapse and increased the 80S monosome peak (Fig. 2A). In contrast, polysomes were largely preserved in cells treated with halofuginone (Fig. 2A). Because halofuginone caused translational repression as measured by metabolic labeling (Fig. 1B), these results demonstrate that halofuginone causes elongating ribosomes to stall on mRNAs.

We next determined whether puromycin could release mRNAs from stalled ribosomes during halofuginone treatment. Puromycin is a small molecule peptidyl-tRNA mimic that causes premature ribosome release when incorporated into nascent chains (Azzam and Algranati 1973). We anticipated that puromycin would enter vacant A sites of ribosomes stalled awaiting

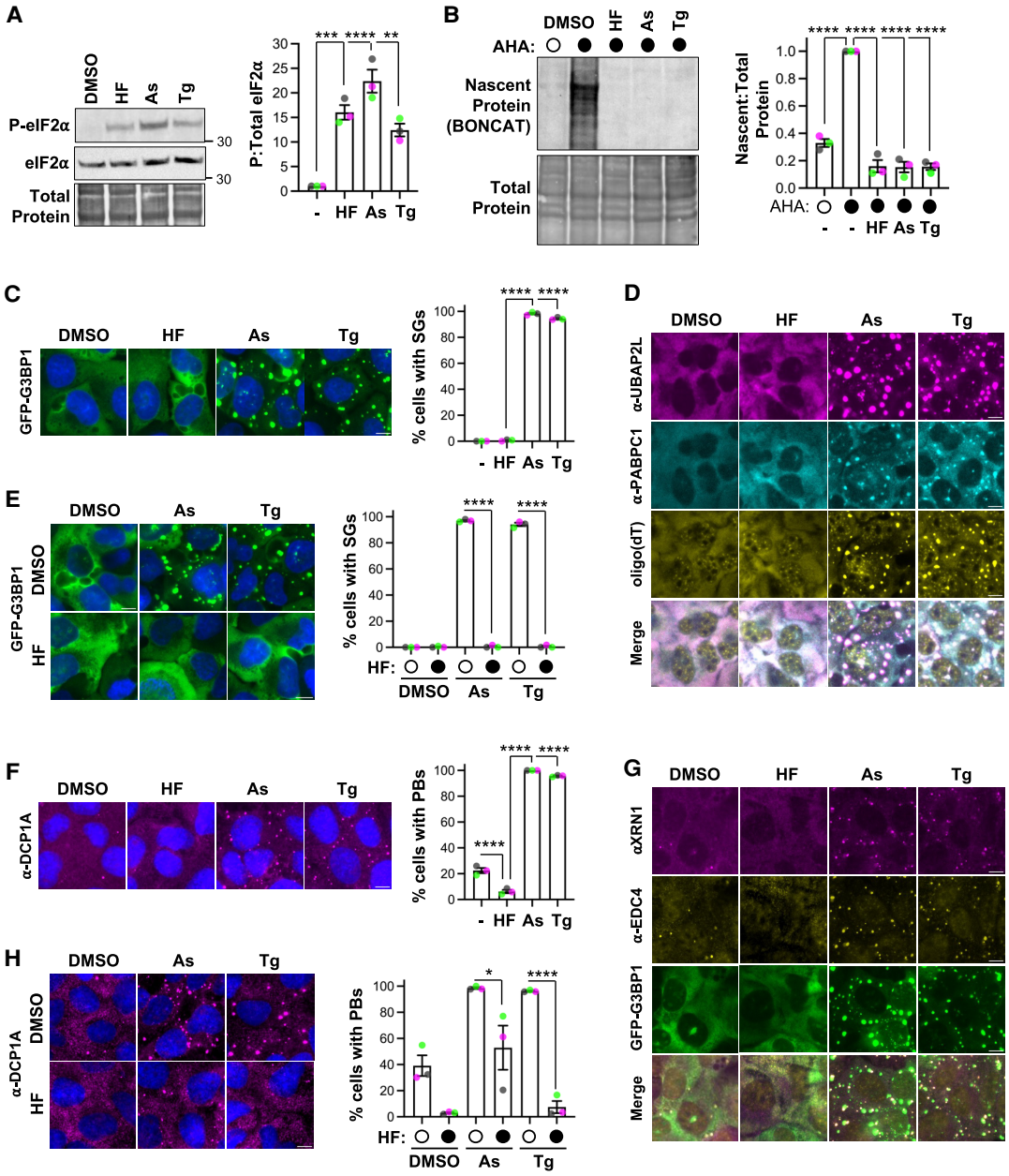

Figure 1. Inhibition of tRNA charging activates the ISR without inducing RNP granules. (*A*) U-2 OS cells were treated with 0.2% DMSO carrier, 20 µM halofuginone (HF), 250 µM sodium arsenite (As), or 1.25 µM thapsigargin (Tg) for 1 h, and Western blotting for phosphorylated and total eIF2α was done. Total protein ($n = 3$ independent replicates) and molecular weights (in kilodaltons) are shown. (*B*) Translation activity was measured using bioorthogonal noncanonical amino acid tagging in cells treated as in *A*. Methionine or azidohomoalanine (AHA) was added 10 min prior to collection. The ratio of nascent to total protein is shown from $n = 3$ independent replicates. (*C*) U-2 OS cells stably expressing GFP-G3BP1 (green) were treated as in *A* and fixed, and nuclei were stained with Hoechst (blue). The percentage of cells with SGs was quantified from $n = 3$ independent experiments; ≥305 cells were counted in each condition. Scale bars, 10 µm. (*D*) Cells were treated as in *C*, and immunofluorescence and fluorescence in situ hybridization were done to detect UBAP2L (magenta), PABPC1 (cyan), and poly(A) RNA with oligo(dT) probes (yellow) ($n = 2$ independent experiments). (*E*) Cells were treated with 0.2% DMSO, 20 µM HF plus 0.2% DMSO, 250 µM arsenite, or 1.25 µM thapsigargin for 1 h, and the percentage of cells with SGs was quantified ($n = 3$ independent experiments); ≥287 cells were counted per treatment. (*F*) Cells were treated, and immunofluorescence microscopy was done as in *D* to detect the P-body marker DCP1A. Quantification of the percentage of cells with P-bodies (PBs) from $n = 3$ independent experiments is shown; ≥364 cells were counted per treatment. (*G*) Cells were treated as in *C* to detect XRN1 (magenta) and EDC4 (yellow) by immunofluorescence microscopy ($n = 2$ independent experiments). (*H*) U-2 OS cells were treated as in *E*, and immunofluorescence microscopy was done to detect DCP1A. The percentage of cells with PBs from $n = 3$ independent experiments is shown; ≥351 cells were counted per treatment across all replicates. Representative images are shown with the average ± SEM for each experiment, and green, gray, and pink points represent the average of each replicate. Statistical significance was assessed with an ordinary one-way ANOVA followed by Tukey's multiple comparisons test. (*) $P < 0.05$, (**) $P < 0.01$, (***) $P < 0.005$, (****) $P < 0.001$.

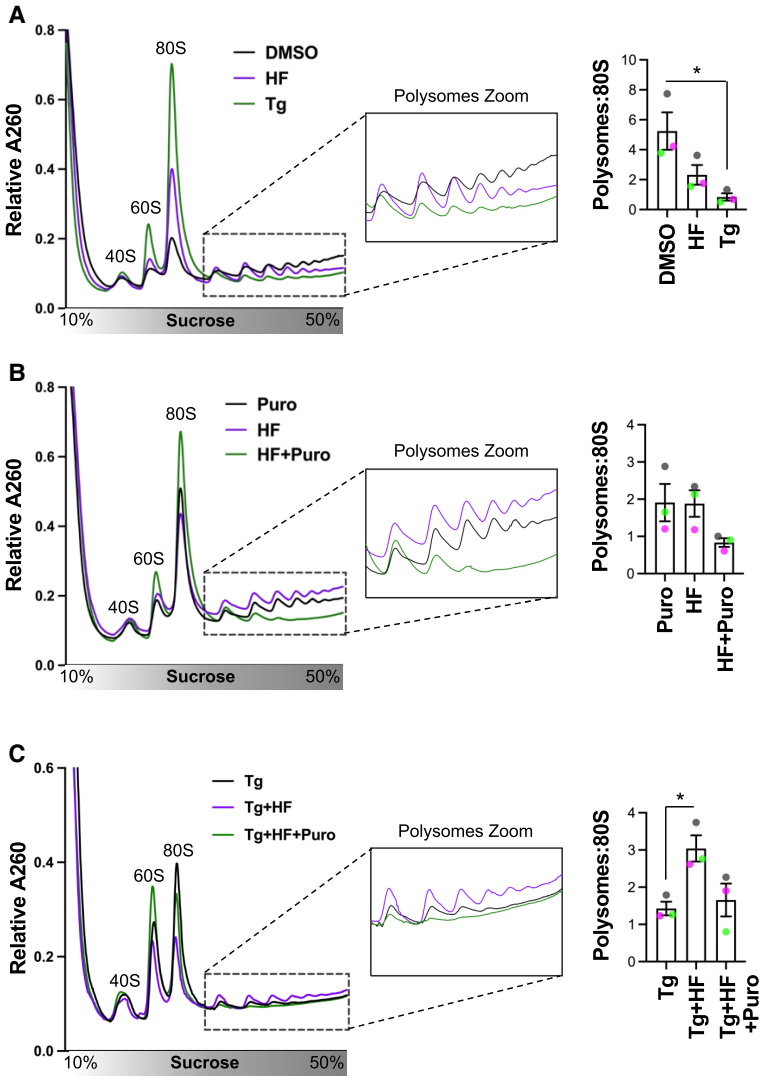

Figure 2. tRNA charging is required for stress-induced mRNA release from polysomes. (*A*) U-2 OS cells were treated with 20 µM halofuginone (HF; purple line), 1.25 µM thapsigargin (Tg; green line), or 0.2% DMSO carrier (black line) for 1 h, and polysome profiling was done; representative profiles are shown at the *left* ($n = 3$ independent experiments). The areas under the polysome fractions and 80S peak were quantified and are shown at the *right*. (*B*) Cells were treated with 10 µg/mL puromycin (black line), 20 µM HF (purple line), or 10 µg/mL puromycin and 20 µM HF (green line) for 1 h, and polysome profiling was performed and quantified as in *A* ($n = 3$ independent experiments). (*C*) Cells were treated with 1.25 µM Tg (black line), 20 µM HF plus 1.25 µM Tg (purple line), or 20 µM HF plus 1.25 µM Tg and 10 µg/mL puromycin (green line), and polysome profiling was done and quantified as in *A* ($n = 3$ independent experiments). The average of three independent experiments with SEM is shown, with the average of each replicate in pink, green, or gray. Significance was assessed with ordinary one-way ANOVAs and Tukey's multiple comparisons tests. (*) $P < 0.05$.

Pro-tRNA^{Pro}, releasing nascent peptides and causing polysome collapse during halofuginone treatment. Puromycin alone did not induce complete polysome collapse after 1 h (Fig. 2B), likely due to continued translation initiation. However, cotreatment of cells with halofuginone and puromycin reduced the polysome fraction, increased the 80S monosome fraction, and decreased the polysome to monosome ratio ~2.4-fold from 1.9 ± 0.4 in cells treated with halofuginone to 0.8 ± 0.1 in cells treated with halofuginone and puromycin (Fig. 2B). Furthermore, halofuginone cotreatment stabilized polysomes in cells treated with thapsigargin, yielding an ~2.1-fold increase in the polysome to monosome ratio from 1.4 ± 0.2 to 3.0 ± 0.4 (Fig. 2C). These observations suggest that halofuginone causes ribosome stalls to persist in the presence of a canonical stressor. Puromycin reversed the effects of halofuginone on the polysome profile in cells treated with thapsigargin and restored the polysome:monosome ratio to 1.7 ± 0.4. These results demonstrate that puromycin rescues ribosome stalling induced by inhibition of tRNA charging by releasing mRNAs from polysomes.

The RQC pathway clears collided disomes but not uncollided stalled ribosomes upon tRNA synthetase inhibition

Because polysomes do not collapse and RNP granules do not assemble upon halofuginone stress, we next asked whether ribosome-associated quality control (RQC) pathways failed to resolve stalled ribosomes that result from uncharged tRNA accumulation. We first assessed whether halofuginone causes ribosome collisions by two approaches. First, we performed disome profiling (Ferguson et al. 2023) and determined whether halofuginone caused RNase-resistant collided ribosomes to accumulate. We found that while disomes were not observed in unstressed cells, halofuginone induced disomes to the same degree as low-dose emetine, an irreversible inhibitor of ribosome translocation (Grollman and Jarkovsky 1975) that causes ribosome collisions (Fig. 3A; Juszkiewicz et al. 2020a; Wu et al. 2020).

Second, we measured ubiquitination of ribosomal protein eS10. The initial stage of the RQC is recognition of

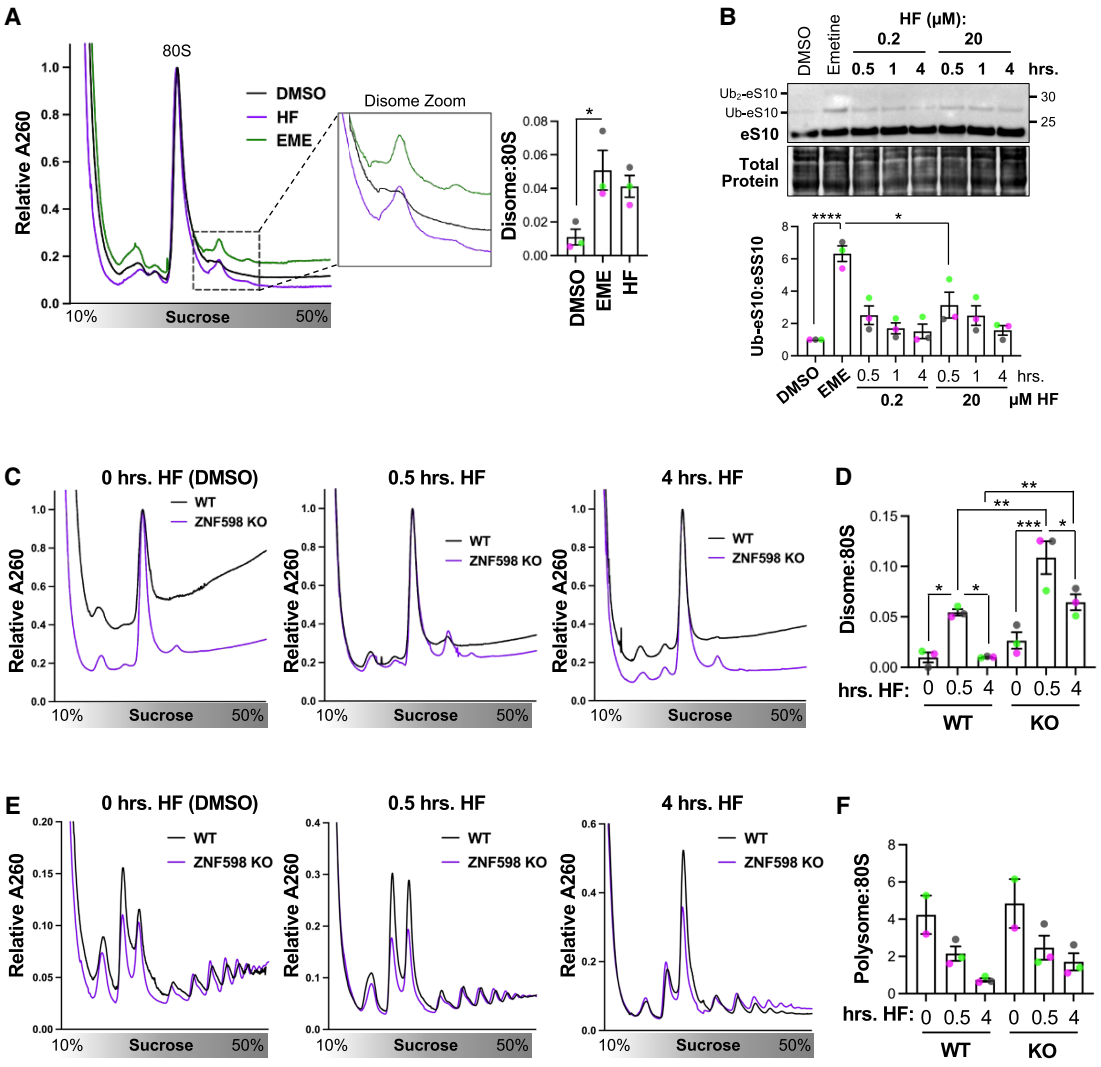

Figure 3. Collided, stalled ribosomes form and are cleared, while isolated stalled ribosomes persist during halofuginone treatment. (*A*) U-2 OS cells were treated with 0.2% DMSO or 20 µM halofuginone (HF) for 30 min or with 0.18 µM emetine (EME) for 15 min. (*Left*) Lysates treated with P1 nuclease were fractionated in sucrose gradients, with relative A260 of representative profiles shown. (*Right*) The average ratio of disomes to monosomes ±SEM from $n = 3$ independent replicates. (*B*) Cells were treated with 0.2% DMSO carrier or 0.18 µM emetine for 15 min or with 0.2 or 20 µM halofuginone (HF) for 0.5, 1, or 4 h, and Western blotting for eS10 was done. The monoubiquitylated (Ub-eS10) and unmodified eS10 bands were quantified; average Ub-eS10:eS10 ratios from $n = 3$ independent experiments are shown at the *bottom*, and a representative blot with total protein and molecular weight (in kilodaltons) is shown at the *top*. (*C*) Representative disome profiles of wild-type or ZNF598 KO cells treated with 0.2% DMSO or 20 µM HF for 0.5 or 4 h. (*D*) Average ± SEM of $n = 3$ independent replicates of disome profiling as in *C*. (*E*) Representative polysome profiles of wild-type or ZNF598 KO cells treated with 0.2% DMSO or 20 µM HF for 0.5 or 4 h. (*F*) Average ± SEM of $n = 3$ independent replicates ($n = 2$ for DMSO controls). Pink, gray, and green points represent each replicate. Significance was determined with ordinary one-way ANOVAs and Tukey's multiple comparisons tests. (*) $P < 0.05$, (**) $P < 0.01$, (***) $P < 0.005$, (****) $P < 0.001$.

the ribosome collision interface and the ubiquitination of ribosomal proteins, including eS10, by the E3 ubiquitin ligase ZNF598 (Juszkiewicz and Hegde 2017; Sundaramoorthy et al. 2017; Juszkiewicz et al. 2018; Goldman et al. 2021; Narita et al. 2022). We observed that treatment with a low concentration of emetine (Juszkiewicz et al. 2020a; Wu et al. 2020) induced robust ubiquitination of eS10, with a 6.3-fold ± 0.5-fold increase over the DMSO carrier control (Fig. 3B). A key observation is that halofuginone increased eS10 ubiquitination by 3.1-fold ± 0.8-fold relative to DMSO controls at 0.5 h, the earliest time point collected (Fig. 3B). These results suggest that the inhibition of tRNA charging leads to ribosome collisions that are recognized by the RQC pathway.

We next evaluated whether stalled, collided ribosomes were cleared over time in cells treated with halofuginone. We performed disome and polysome profiling in untreated cells and cells treated with halofuginone for 0.5 or 4 h.

While disomes were observed at 0.5 h of halofuginone treatment, they were no longer present at 4 h (Fig. 3C, D). In parallel, polysome profiling experiments showed that polysomes are present at 0.5 and 4 h of halofuginone treatment (Fig. 3E,F). These results indicate that disomes, but not uncollided stalled ribosomes, are cleared during tRNA synthetase inhibition.

We next assessed whether stalled ribosomes are cleared through the RQC pathway upon tRNA synthetase inhibition. We compared the level of disomes in wild-type cells treated with halofuginone versus those in cells lacking ZNF598, which initiates the RQC pathway (Juszkiewicz and Hegde 2017). We generated a genetically depleted *ZNF598* knockout U-2 OS cell pool (ZNF598 KO) using CRISPR/Cas9. We verified that *ZNF598* was knocked out by performing Sanger sequencing of the genomic DNA (Supplemental Fig. S3A) and ICE (inference of CRISPR edits) analysis (Supplemental Fig. S3B). Furthermore, while Western blotting with a ZNF598 antibody showed residual expression of a lower-molecular-weight protein in the knockout pool, emetine treatment did not cause Ub-eS10 levels to increase in these cells, suggesting that this lower-molecular-weight ZNF598 protein may be a nonfunctional in-frame deletion (Supplemental Fig. S3C). We observed that robust disomes were formed in cells depleted of ZNF598 upon halofuginone treatment at 0.5 and 4 h, and disome peaks were larger in *ZNF598* knockout cells than in wild-type cells (Fig. 3C,D). However, *ZNF598* knockout did not affect the polysomes that persisted in halofuginone-treated cells at 0.5 or 4 h (Fig. 3E,F). These results indicate that the RQC machinery clears stalled, collided ribosomes that accumulate upon tRNA synthetase inhibition but does not recognize or clear uncollided, stalled ribosomes.

Ribosome collisions contribute to activation of the ISR by halofuginone

We next asked whether ribosome collisions contribute to ISR activation by halofuginone. Uncharged tRNAs and stalled ribosomes can activate the ISR via GCN2 (Wek et al. 1989, 1995; Dong et al. 2000; Sundrud et al. 2009; Keller et al. 2012; Lageix et al. 2015; Harding et al. 2019; Kim et al. 2020b; Wu et al. 2020; Pitera et al. 2022; Stoneley et al. 2022; Misra et al. 2024; Sinha et al. 2024). We assessed P-eIF2α levels in cells treated with halofuginone, arsenite, or thapsigargin in the presence or absence of puromycin to prevent ribosome collisions by releasing mRNAs from ribosomes (Misra et al. 2024). We found that while halofuginone significantly increased P-eIF2α levels, the addition of puromycin reduced the levels of P-eIF2α by approximately twofold (Fig. 4A). In contrast, P-eIF2α levels did not change upon puromycin cotreatment with arsenite or thapsigargin. These results suggest that ribosome occupancy contributes to, but is not solely responsible for, activation of the ISR after loss of tRNA charging.

Because the RQC pathway resolves ribosome collisions, we hypothesized that activation of RQC by halofuginone would limit GCN2 activation and reduce P-eIF2α levels. We reasoned that P-eIF2α levels resulting from collisions would be elevated in cells that cannot clear collided ribosomes due to genetic depletion of *ZNF598*. We assessed P-eIF2α levels in wild-type and *ZNF598* KO cells treated with halofuginone at 0.5, 1, and 4 h. At 4 h after halofuginone treatment, *ZNF598* KO cells had a significant, 1.63-fold increase in P-eIF2α compared with wild-type cells (Fig. 4B). No significant differences in P-eIF2α were observed early in stress (Fig. 4B). Therefore, ZNF598 limits activation of the ISR when tRNA charging is inhibited.

We hypothesized that the observed increase in P-eIF2α levels during halofuginone treatment in the *ZNF598* KO cell line was due to the accumulation of ribosome collisions, which would otherwise be cleared by the RQC pathway. We performed two experiments to test this hypothesis. First, we assessed whether stalled ribosomes contributed to the elevated P-eIF2α levels observed in *ZNF598* KO cells. We cotreated wild-type and *ZNF598* KO cells with puromycin during 1 or 4 h of halofuginone stress to resolve stalled ribosomes and assessed P-eIF2α levels. We found that puromycin reduced P-eIF2α levels in *ZNF598* KO cells to levels comparable with those observed in wild-type cells treated with halofuginone alone (Fig. 4C). There was no statistically significant difference in P-eIF2α levels between wild-type cells treated with halofuginone and *ZNF598* KO cells treated with halofuginone and puromycin at the 4 h time point. This result suggests that the increased P-eIF2α levels in *ZNF598* KO cells resulted from persistent collided ribosomes that would otherwise be cleared by the RQC pathway.

Second, we assessed how the levels of CReP and GADD34, which interact with protein phosphatase 1 to dephosphorylate P-eIF2α, contribute to P-eIF2α levels throughout the duration of halofuginone treatment. We reasoned that *ZNF598* KO cells could display an increase in P-eIF2α during late (4 h) halofuginone stress compared with wild-type cells if CReP and GADD34 were depleted more in the absence of ZNF598 at that time point. Wild-type cells would otherwise have sufficient P-eIF2α phosphatase activity to limit P-eIF2α levels during halofuginone stress. Our data rule this possibility out, as we found that GADD34 and CReP are equally reduced during halofuginone stress in *ZNF598* KO and wild-type cells (Fig. 4D). The observed reduction in CReP and GADD34 levels is in line with the results of prior studies that demonstrated that CReP is rapidly depleted upon translation suppression (Misra et al. 2024) and that GADD34 and CReP are not expressed in cells treated with high levels of halofuginone (Pitera et al. 2022). Not all proteins were depleted at 4 h after halofuginone treatment, as tubulin and total protein levels were unchanged over time (Fig. 4D). Thus, CReP and GADD34 levels are equivalent in wild-type and *ZNF598* KO cells throughout the duration of treatment. Taken together, these results demonstrate that ribosome collisions occur during tRNA synthetase inhibition, contribute to increased P-eIF2α levels, and do so via increased phosphorylation of eIF2α and not through decreased phosphatase levels.

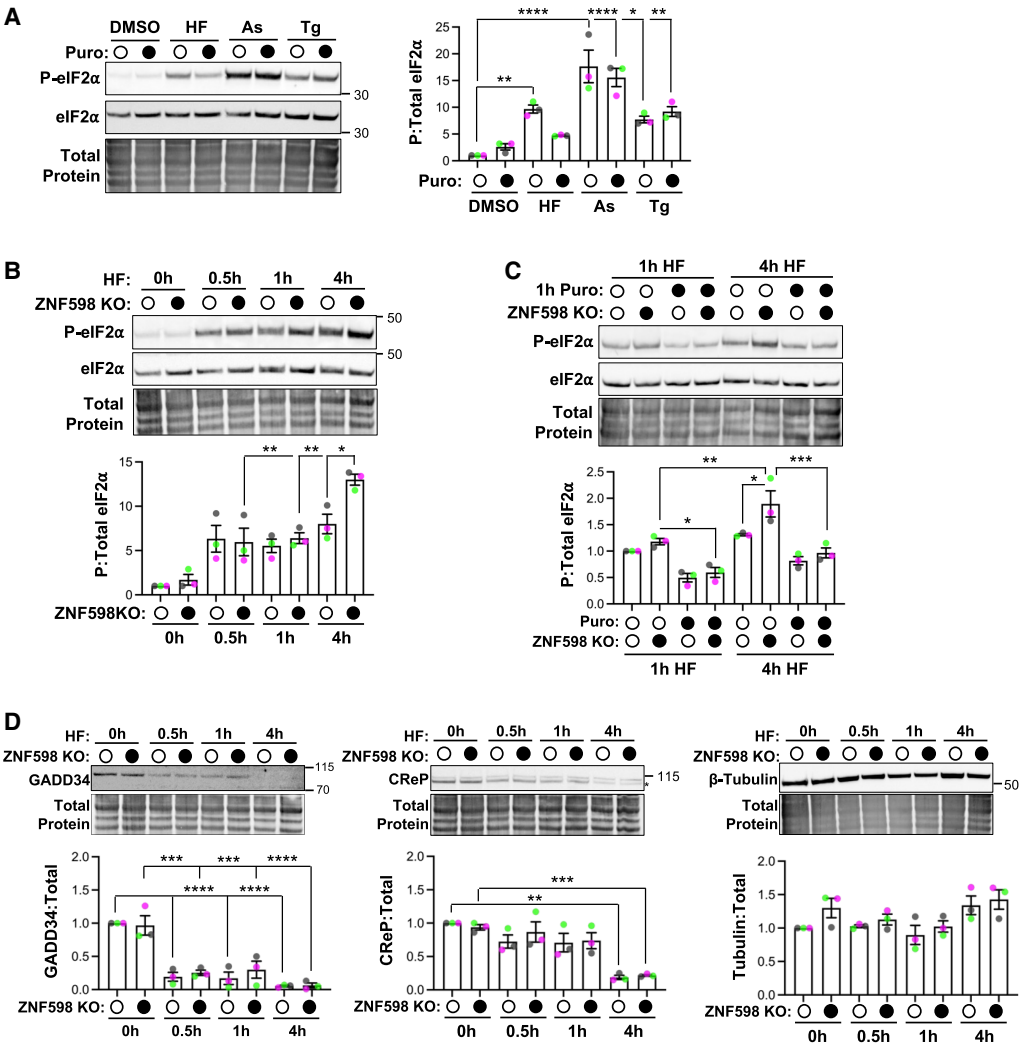

Figure 4. Ribosome collisions contribute to ISR activation during halofuginone treatment. (*A*) Cells were treated with 0.2% DMSO, 20 µM halofuginone (HF), 250 µM sodium arsenite (As), or 1.25 µM thapsigargin (Tg) with or without 10 µg/mL puromycin (Puro) for 1 h, and P-eIF2α and total eIF2α levels were determined by Western blotting. Quantification of P-eIF2α:eIF2α is shown at the *right*, and a representative blot with total protein from $n = 3$ independent experiments shown at the *left*. (*B*) Western blotting of total and P-eIF2α was done from wild-type (WT) and *ZNF598* knockout (KO) cells treated with 20 µM HF for 0.5, 1, or 4 h. A representative blot with total protein is shown (*top*), and results from $n = 3$ independent replicates were quantified (*bottom*). (*C*) Western blotting of P-eIF2α and total eIF2α from WT and *ZNF598* KO cells treated with 20 µM HF for 1 or 4 h in the absence or presence of 10 µg/mL puromycin added 1 h prior to collection. Representative blot with total protein from $n = 3$ independent experiments (*top*) and quantification of P-eIF2α:eIF2α (*bottom*) are shown. (*D*) Wild-type and *ZNF598* KO cells were treated as in *B*, and Western blotting for GADD34, CReP (marked by an asterisk), and β-tubulin was done with quantification relative to total protein. Representative blots are shown at the *top*, and results from $n = 3$ independent experiments are shown *below*. Molecular weights (in kilodaltons) are indicated on each blot. Quantification is reported as average ± SEM, with pink, gray, and green points representing each replicate. Statistical significance was determined with ordinary one-way ANOVAs and Tukey's multiple comparisons tests. (*) $P < 0.05$, (**) $P < 0.01$, (***) $P < 0.005$, (****) $P < 0.001$.

Inducing ribosome release rescues RNP granule assembly after tRNA synthetase inhibition

We next asked whether unresolved ribosome stalls block RNP granule assembly when tRNA synthetase activity is inhibited during stress. First, we assessed whether stabilizing ribosomes on mRNAs during translation elongation prevented stress-induced RNP granule assembly. Consistent with past research (Kedersha et al. 2000, 2005; Mollet et al. 2008; Khong and Parker 2018; Helton et al. 2025), trapping mRNAs in polysomes with the irreversible ribosome translocation inhibitor emetine (Grollman and Jarkovsky 1975) prevents SGs from forming during arsenite stress (Fig. 5A). Emetine also significantly reduced PBs in unstressed cells (Fig. 5A). While we observed that emetine significantly reduced the size and number of PBs during arsenite stress (Supplemental Fig. S4A,B), it did not change the percentage of cells with PBs, similar to prior results of experiments with the translation elongation inhibitor cycloheximide (Fig. 5A; Sheth and Parker 2003;

Cougot et al. 2004; Kedersha et al. 2005; Teixeira et al. 2005; Mollet et al. 2008). Therefore, blocking translation elongation inhibits stress granule and constitutive P-body assembly.

To directly test whether ribosome stalling during tRNA synthetase inhibition prevents RNP granule assembly, we used puromycin to release mRNAs from ribosomes during halofuginone treatment and evaluated SG and PB formation. While SGs were not observed in halofuginone treatment alone, cotreatment with puromycin and halofuginone for 1 h caused SG assembly in 60.5% ± 2.0% of cells (Fig. 5B). Puromycin did not cause SG assembly in unstressed cells or alter SG assembly upon treatment with arsenite or thapsigargin (Fig. 5B). Similarly, while SGs did not form in the presence of halofuginone during either arsenite or thapsigargin stress, puromycin cotreatment rescued SG assembly (Fig. 5C).

We next determined whether P-bodies are also limited by mRNA retention in polysomes upon halofuginone treatment. Puromycin cotreatment significantly increased the percentage of cells with PBs, from 5.1% ± 2.7% in cells treated with halofuginone alone to 54.8% ± 6.1% in cotreated cells (Fig. 5D). In contrast to what was observed with emetine treatment, halofuginone blocked the assembly of P-bodies upon arsenite or thapsigargin stress (Fig. 5E). Cotreatment with puromycin also rescued PB assembly in cells treated with halofuginone and arsenite or thapsigargin (Fig. 5E). Specifically, the percentage of cells with PBs increased from 20.2% ± 4.8% in cells with arsenite and halofuginone to 99.4% ± 0.4% when puromycin was added and from 11.1% ± 3.8% in cells with thapsigargin and halofuginone to 95.1% ± 2.2% upon addition of puromycin. Together, these results suggest that RNP granules do not assemble when tRNA charging is impaired because stalled ribosomes remain associated with mRNAs.

One alternative possibility is that puromycin drives RNP granule assembly by increasing ISR activation in halofuginone-treated cells. Puromycin can induce SGs at high concentrations or during long treatment (i.e., 24 h) (Kedersha et al. 2000; Martinez et al. 2016; Markmiller et al. 2018) and increases P-eIF2α levels in association with reduced CReP expression (Misra et al. 2024). We found that Ub-eS10 levels suggestive of ribosome collisions are elevated early in halofuginone stress (Fig. 3B) at similar times when GADD34 and CReP are at their highest levels during halofuginone treatment (Fig. 4D). If ribosome collisions contribute to P-eIF2α levels early during halofuginone treatment, we reasoned that puromycin cotreatment would reduce P-eIF2α levels by resolving stalled, collided ribosomes that activate GCN2. We therefore assessed P-eIF2α levels in cells treated with halofuginone in the presence or absence of puromycin over a 4 h time course. Consistent with the idea that puromycin releases stalled, collided ribosomes from mRNAs that contribute to ISR activation, we observed that puromycin reduced P-eIF2α levels early, but not late, during halofuginone treatment (Supplemental Fig. S5A). We also assessed SG assembly over the same time course of halofuginone treatment in the presence or absence of puromycin. A key observation was that fewer cells formed SGs early during halofuginone and puromycin cotreatment versus longer-term treatment (Supplemental Fig. S5B). The percentage of cells with SGs increased over time in cells treated with halofuginone and puromycin, from 35.5% ± 2.0% of cells with SGs after 1 h of cotreatment to 94.7% ± 2.5% of cells with SGs after 4 h of cotreatment (Supplemental Fig. S5B). Together, these observations are consistent with the idea that puromycin minimizes ISR activation early in halofuginone stress and limits SG assembly by preventing ribosome collisions and promotes SG assembly later during halofuginone stress by releasing mRNAs from stalled ribosomes.

Halofuginone specifically inhibits the prolyl-tRNA synthetase activity of EPRS1 (Keller et al. 2012) and does not affect the extent of charging by other tRNA synthetases (Misra et al. 2024). We therefore tested whether inhibiting tRNA charging of other amino acids also blocked the assembly of SGs and PBs through ribosome stalling. To do so, we treated cells with borrelidin, which inhibits threonyl-tRNA synthetase (Paetz and Nass 1973) and also activates the ISR via GCN2 (Sidhu et al. 2015). We found that borrelidin induced levels of P-eIF2α similarly to thapsigargin, with a 10.4-fold ± 1.4-fold increase of borrelidin over control versus a 11.1-fold ± 0.6-fold increase with thapsigargin (Supplemental Fig. S6A). Consistent with our previous findings with halofuginone, no SGs were observed in cells treated with borrelidin, and borrelidin inhibited thapsigargin-induced SGs (Supplemental Fig. S6B). Furthermore, puromycin cotreatment rescued SG assembly in cells treated with borrelidin (to 77.9% ± 4.6% of cells), and puromycin also rescued SG assembly in cells stressed with thapsigargin and borrelidin (Supplemental Fig. S6 B,C). Similarly, the percentage of cells with PBs was decreased from 30.4% ± 7.4% in unstressed cells to 2.8% ± 0.8% during borrelidin treatment and was restored to 20.9% ± 4.9% by puromycin. Borrelidin also decreased the percentage of cells with PBs during thapsigargin treatment from 99.3% ± 0.7% to 5.1% ± 1.9%, an effect that was rescued to 94.8% ± 1.9% by puromycin (Supplemental Fig. S6B,D). Therefore, the uncoupling of RNP granule assembly from the ISR is generalizable across multiple tRNA charging inhibitors.

tRNA synthetase inhibition causes persistent ribosome stalls

Multiple cellular mechanisms exist to resolve ribosomes stalled in elongation, including RQC and ribosome rescue factors related to the translation termination machinery (D'Orazio and Green 2021; Yip and Shao 2021). We therefore hypothesized that ribosome stalls caused by tRNA charging inhibition would eventually be removed from mRNAs and enable RNP granule assembly. We first assessed whether SGs were formed during long-term tRNA charging inhibition using live-cell imaging of the SG marker GFP-G3BP1 in cells treated with halofuginone. We found that halofuginone-treated cells did not form SGs for up to 16 h of treatment, the limit of imaging before cytotoxicity was observed (Fig. 6A). The absence of SGs was not due to detoxification of halofuginone or resolution of stress, as

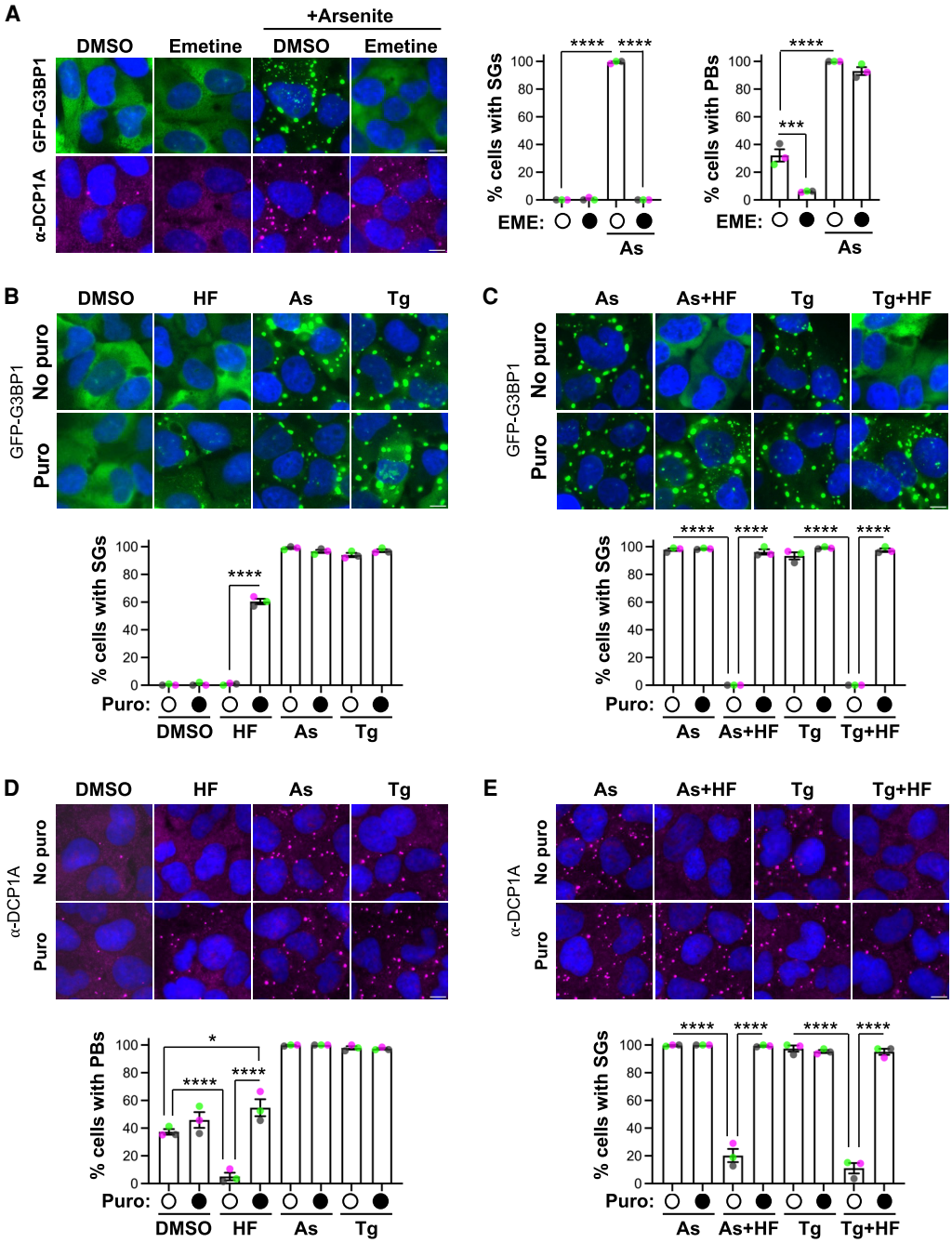

Figure 5. Ribosome release rescues stress-induced RNP granule assembly upon tRNA synthetase inhibition. (*A*) U-2 OS cells stably expressing GFP-G3BP1 were treated with 180 µM emetine (eme) or 0.2% DMSO with 250 µM sodium arsenite (As) for 1 h. Immunofluorescence microscopy was performed for P-body (PB) marker DCP1A, and the SG marker GFP-G3BP1 was imaged. (*Right*) The percentage of cells with SGs or PBs was quantified from $n = 3$ independent experiments; ≥349 cells were counted per treatment across all replicates. (*B*) Cells were treated with 0.2% DMSO, 20 µM HF, 250 µM As, or 1.25 µM thapsigargin (Tg) with or without 10 µg/mL puromycin for 1 h, followed by imaging and quantification of SGs. The percentage of cells with SGs was quantified from $n = 3$ independent experiments (*bottom*), and representative images are shown (*top*); ≥350 cells were counted per treatment across all replicates. (*C*) Cells were treated with 20 µM HF in the presence or absence of 250 µM As, 1.25 µM Tg, or 10 µg/mL puromycin for 1 h. The percentage of cells with SGs was quantified from $n = 3$ independent experiments; ≥290 cells were counted per treatment across all replicates. (*D*) Cells were treated as in *B*, and IF for DCP1A was performed. The percentage of cells with P-bodies (PBs) was quantified from $n = 3$ independent experiments (*bottom*), and representative images are shown (*top*); ≥355 cells were counted per treatment across all replicates. (*E*) Cells were treated as in *C*, and IF was performed to detect DCP1A. The percentage of cells with PBs was quantified from $n = 3$ independent experiments (*bottom*), and representative images are shown (*top*); ≥339 cells were counted per treatment across all replicates. Quantification is reported as average ± SEM, with green, pink, or gray dots indicating the average of each replicate. Scale bars, 10 µm. Statistical significance was assessed with an ordinary one-way ANOVA followed by Tukey's multiple comparisons test. (*) $P < 0.05$, (***) $P < 0.005$, (****) $P < 0.001$.

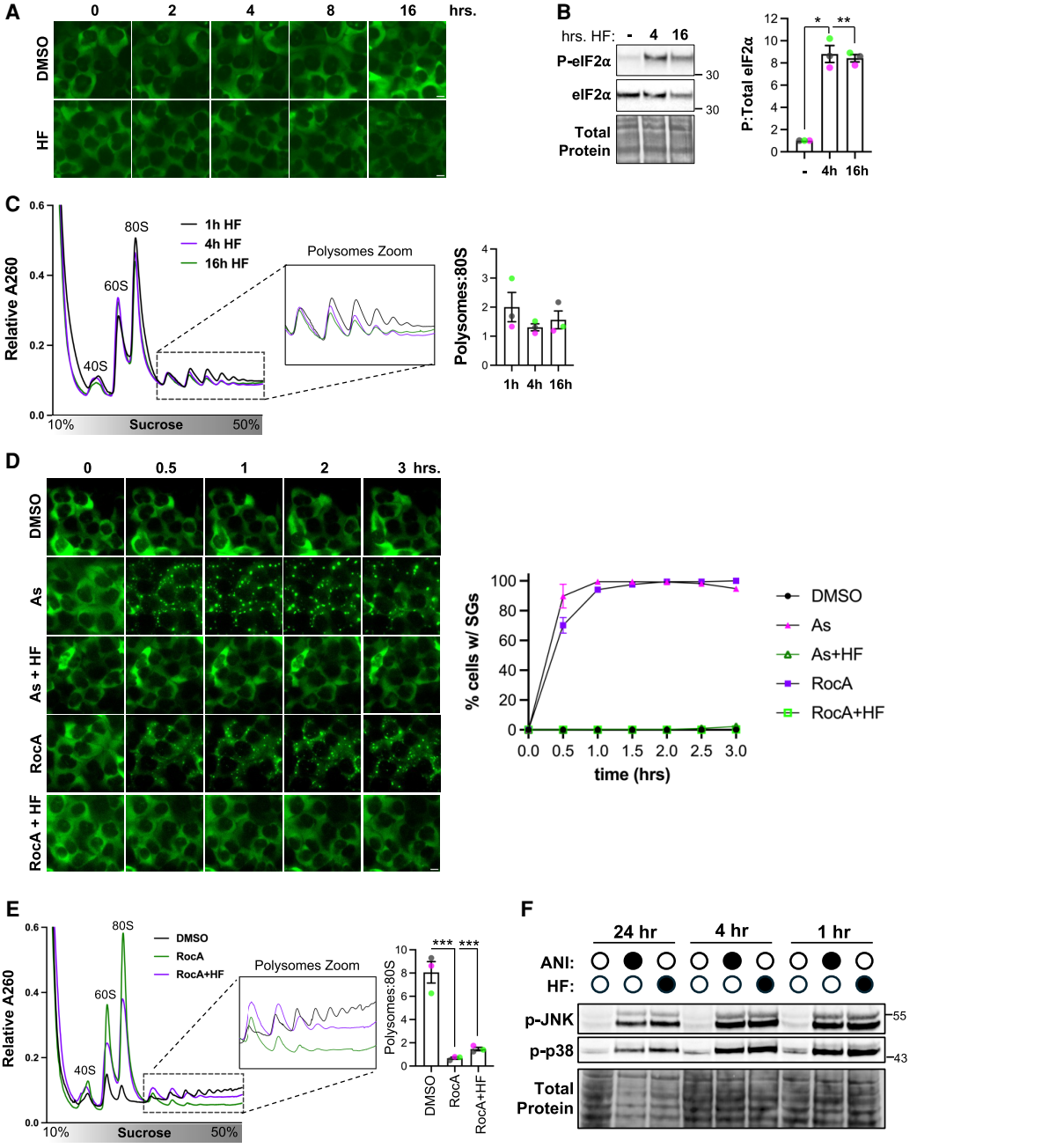

Figure 6. tRNA synthetase inhibition causes persistent ribosome stalls. (*A*) U-2 OS cells expressing GFP-G3BP1 were treated with 20 µM halofuginone (HF) or 0.2% DMSO carrier. Images were collected every 2 h for 16 h and representative images are shown ($n = 3$ independent experiments). (*B*) Cells were treated with DMSO (–) or 20 µM HF for 4 or 16 h, and P-eIF2α and total eIF2α were detected by Western blotting. Representative blots with total protein are shown at the *left*, and the average ± SEM of $n = 3$ independent experiments is shown at the *right*. Molecular weights (in kilodaltons) are shown. (*C*) Cells were treated with 20 µM HF for 1 h (black line), 4 h (purple line), or 16 h (green line), and polysome profiling was performed. A representative profile is shown at the *left*, and the average ± SEM of the polysome:monosome ratio from $n = 3$ independent replicates is shown at the *right*. Pink, gray, and green dots represent results from each replicate. (*D*) Cells were treated with either 0.2% DMSO carrier or 20 µM HF in the presence or absence of 250 µM sodium arsenite (As) or 2 µM rocaglamide A (RocA), and GFP-G3BP1 was imaged every 0.5 h for 3 h. Representative images are shown at the *left* with the average ± SEM. The percentage of cells with SGs from $n = 3$ independent experiments is shown at the *right*; ≥288 cells were counted per treatment across all replicates. (*E*) Cells were treated with 0.2% DMSO (black line), 2 µM RocA (green line), or 2 µM RocA plus 20 µM HF (purple line) for 3 h followed by polysome profiling. Representative profiles are shown at the *left*, and the average ± SEM from $n = 3$ independent experiments is shown at the *right*, with pink, gray, and green dots representing each replicate. (*F*) Cells were untreated (DMSO carrier) or treated for 24, 4, or 1 h with 20 µM anisomycin (ANI) or 20 µM halofuginone, and Western blotting for p-p38 and p-JNK was done, with the total protein shown *below*. A representative blot of $n = 2$ independent experiments is shown. Scale bars, 10 µm. Significance was assessed with ordinary one-way ANOVAs and Tukey's multiple comparisons tests. (*) $P < 0.05$, (**) $P < 0.01$, (***) $P < 0.005$.

P-eIF2α levels remained high at 16 h (Fig. 6B). Additionally, polysome profiling confirmed that polysomes persist at 16 h of stress (Fig. 6C). Furthermore, the levels of rRNA over the 16 h time course remained unchanged (Supplemental Fig. S7A), suggesting that ribosomes are not cleared through the nonfunctional rRNA decay pathway as occurs in yeast (Li et al. 2022). Similarly, assessment of bulk RNA stability using actinomycin D transcriptional shutoff and oligo(dT) FISH in cells treated with either DMSO (carrier) or halofuginone for 4 h (when translation initiation and elongation are inhibited) demonstrated that halofuginone does not trigger global mRNA decay, which could occur due to mRNA surveillance pathways when elongation is impaired (Supplemental Fig. S7B). These results suggest that ribosome stalls due to the loss of tRNA charging are cleared either very slowly or not at all.

One alternative possibility is that ribosome stalls are cleared but are also slowly replaced by residual translation initiation activity. To test this possibility, we performed live-cell imaging of GFP-G3BP1-expressing cells treated with halofuginone and either arsenite or rocaglamide A, which inhibit translation initiation via the ISR or eIF4A inhibition (Sadlish et al. 2013), respectively. We found that while robust SG assembly occurred in rocaglamide A-treated or arsenite-treated cells, halofuginone completely prevented SG formation in cells cotreated with rocaglamide A or arsenite up to 3 h later (the duration of imaging) (Fig. 6D). In line with these results, halofuginone limited polysome collapse upon rocaglamide A treatment (Fig. 6E). Specifically, after 3 h of treatment, the polysome to 80S ratio was increased ~2.1-fold, from 0.7 ± 0.1 in cells treated with rocaglamide A alone to 1.5 ± 0.2 in cells cotreated with rocaglamide A and halofuginone. These results suggest that the ribosomes associated with mRNAs after long-term halofuginone treatment are stable, stalled species rather than the result of continued translation initiation.

We next determined whether the ribotoxic stress response pathway is triggered upon tRNA synthetase inhibition. The RSR is activated by collided disomes and, to a lesser extent, in conditions such as amino acid deprivation or treatment with translation inhibitors (e.g., lactimidomycin) in which ribosomes stall but collisions are not detectable (Darnell et al. 2018; Vind et al. 2020a,b; Wu et al. 2020; Snieckute et al. 2022). We performed Western blotting to detect two RSR-activated MAP kinases—phosphorylated p38 (p-p38) and p-JNK (phosphorylated c-Jun N-terminal kinase)—in lysates of cells treated with halofuginone or the RSR activator anisomycin (equimolar to halofuginone) (Iordanov et al. 1997; Vind et al. 2020b; Sinha et al. 2024) for 1, 4, and 24 h. Intriguingly, the ribotoxic stress response was persistently activated with halofuginone or equimolar anisomycin treatment (Fig. 6F). Therefore, chronic tRNA synthetase inhibition persistently activates the ribotoxic stress response.

Amino acid deprivation uncouples stress granules from the ISR

We next asked whether inhibited RNP granule assembly associated with prolonged ribosome stalling was generalizable to other stress conditions by testing whether amino acid deprivation also induced the ISR without causing RNP granule assembly. Prior studies showed that amino acid deprivation activates the ISR via GCN2 (Dever et al. 1992; Wek et al. 1995; Harding et al. 2000, 2019; Darnell et al. 2018) and results in ribosome stalling and uncharged tRNA accumulation (Harding et al. 2000, 2019; Zaborske et al. 2009; Darnell et al. 2018; Wu et al. 2020). We deprived cells of arginine or glutamine for 1, 4, and 16 h and assessed P-eIF2α levels compared with controls in complete media. We observed that P-eIF2α levels were significantly increased in cells deprived of arginine (Fig. 7A) or glutamine (Fig. 7B). We next evaluated SG and PB assembly by imaging GFP-G3BP1 and DCP1A using immunofluorescence microscopy. Strikingly, we observed that SGs were not induced in cells starved of arginine (Fig. 7C) or glutamine (Fig. 7D) at any time point. However, we observed that PBs were assembled in cells deprived of arginine or glutamine, which was similar to the effects of emetine treatment during arsenite stress. The percentage of cells with PBs increased early during arginine (Fig. 7C) or glutamine deprivation (Fig. 7D) and returned to baseline at 4 or 16 h, respectively. We ruled out the possibility that P-eIF2α levels were too low during arginine or glutamine deprivation to induce stress granules, as upon amino acid deprivation P-eIF2α was induced to an extent similar to that in treatment with thapsigargin (Fig. 7E), and thapsigargin caused robust SG and PB assembly (Fig. 7F). Therefore, amino acid deprivation also uncouples stress granule assembly from the ISR.

Discussion

We showed that tRNA charging is essential for stress-induced RNP granule assembly by preventing persistent, unresolved ribosome stalling. Prolyl-tRNA and threonyl-tRNA synthetase inhibitors induce the ISR yet block RNP granule formation by trapping mRNAs in stalled ribosomes. Similarly, amino acid deprivation activates the ISR without causing SG assembly. We further observed disome formation and RQC pathway activation via ZNF598 and showed that collided disomes are cleared early upon tRNA synthetase inhibition. Analysis of P-eIF2α in wild-type and ZNF598-depleted cells treated with puromycin demonstrated that ribosome collisions make a minor contribution to ISR activation when tRNA charging is inhibited. Additionally, we showed that the RSR is robustly and persistently activated by tRNA synthetase inhibition. Together, these results indicate that inhibition of tRNA charging uncouples RNP granule formation from the ISR due to persistently stalled ribosomes (Fig. 8). To our knowledge, this is the first study to demonstrate that these uncollided, stalled ribosomes persist during tRNA synthetase inhibition and are refractory to RQC pathways.

Here we provide strong evidence that ribosome collisions arise rapidly during tRNA synthetase inhibition and are cleared long before uncollided, stalled ribosomes. We directly demonstrated that disomes are formed by 30

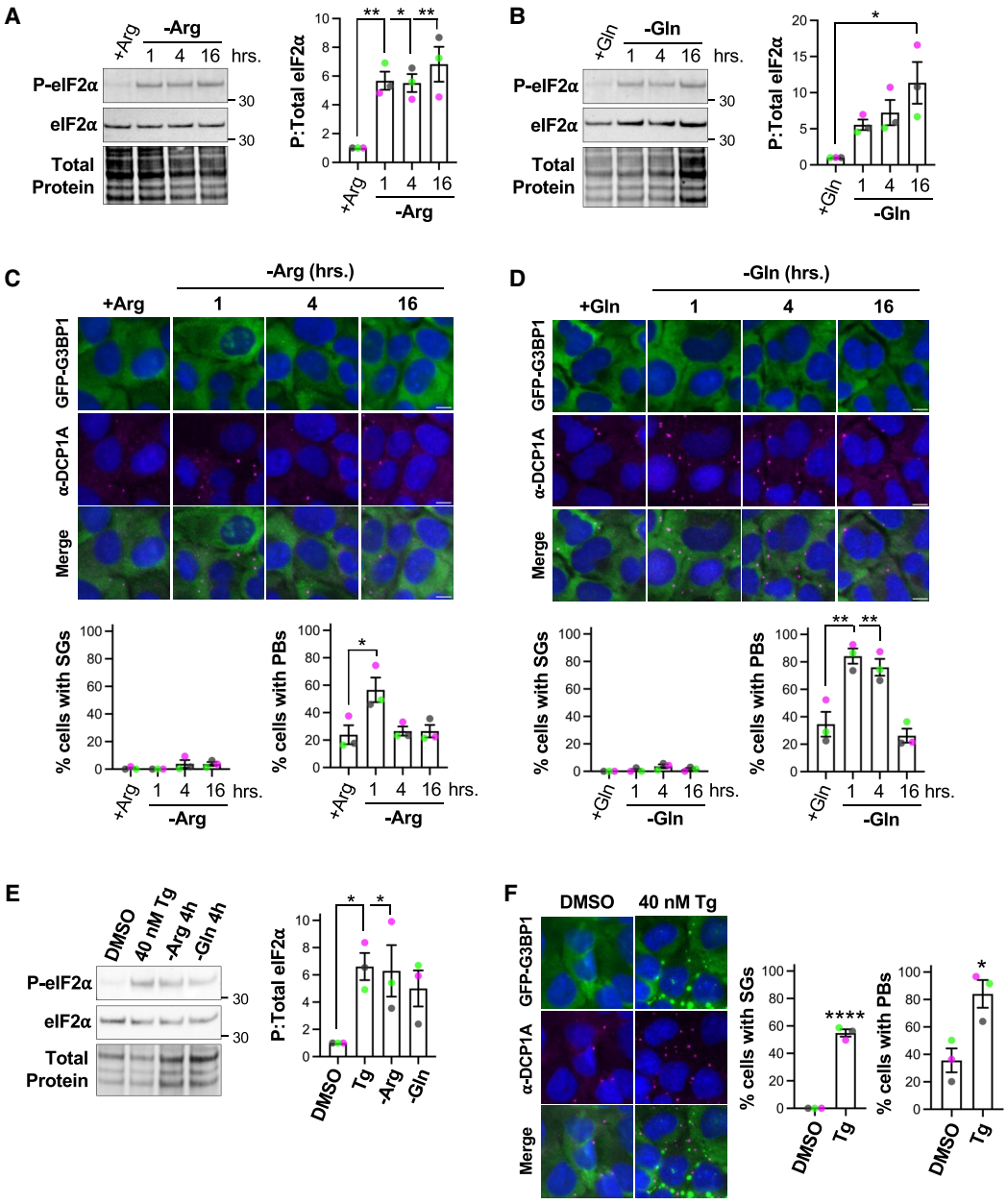

Figure 7. Amino acid deprivation activates the integrated stress response without inducing stress granules. (*A*) U-2 OS cells were placed in media without arginine (−Arg) for 1, 4, or 16 h or in the same media with arginine added back (+Arg) for 4 h, and a representative Western blot for total and P-eIF2α with total protein is shown. (*B*) As in *A*, with glutamine (Gln)-free media or with glutamine added back (+Gln). (*C*) U-2 OS cells stably expressing GFP-G3BP1 (green) were treated as in *A*, followed by immunofluorescence for P-body (PB) marker DCP1A (magenta), and nuclei were stained with Hoechst (blue). The percentages of cells with stress granules (SGs) and PBs were quantified from $n = 3$ independent experiments; ≥410 cells were counted for each condition. (*D*) As in *C* but with glutamine deprivation; ≥312 cells were counted for each condition. (*E*) Cells were treated with DMSO or 40 nM thapsigargin (Tg) for 1 h or starved of arginine or glutamine for 4 h followed by Western blotting for total or P-eIF2α, with total protein shown *below*. (*F*) GFP-G3BP1-expressing U-2 OS cells were treated with DMSO control or 40 nM Tg for 1 h, and immunofluorescence was done for DCP1A. The average percentage of cells with SGs or PBs is shown at the *right*; ≥440 cells were counted per treatment. Scale bars, 10 µm. Molecular weights (in kilodaltons) are shown on each blot. Images are shown for each experiment ($n = 3$ independent replicates), with quantifications reported as average ± SEM and with green, gray, and pink points representing the value for each replicate. Statistical significance was assessed with an ordinary one-way ANOVA followed by Tukey's multiple comparisons test for all but *F*, where a *t*-test was used. (*) $P < 0.05$, (**) $P < 0.01$, (****) $P < 0.001$.

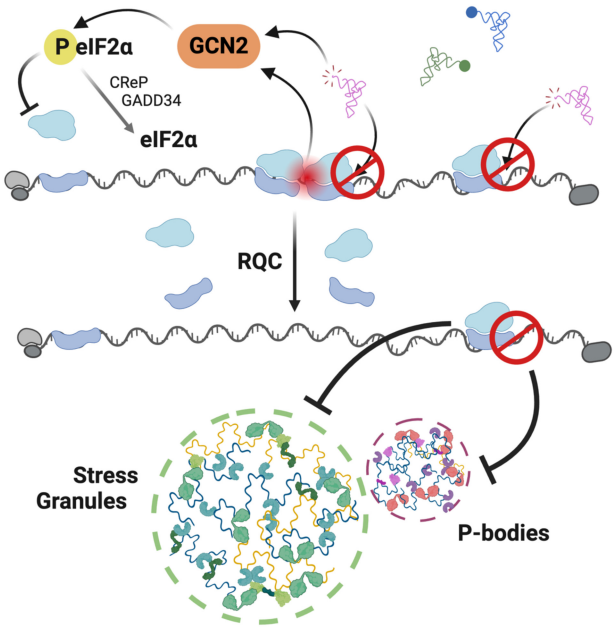

Figure 8. Model depicting the requirement of tRNA synthetase activity for RNP granule assembly. Upon tRNA synthetase inhibition, ribosomes stall, and eIF2α phosphorylation results from uncharged tRNAs and collided ribosomes. Ribosome-associated quality control (RQC) clears stalled, collided ribosomes but cannot resolve ribosomes that stall in the absence of collisions. The association of stalled ribosomes with mRNAs blocks the assembly of stress granules and P-bodies.

min and are undetectable within 4 h of tRNA synthetase inhibition. This time line is consistent with live-cell single-mRNA imaging assays that showed that stalled ribosomes are released from ~50% of mRNAs containing internal poly(A) tracts within 15 min (Goldman et al. 2021). We demonstrated that the RQC pathway, initiated by ZNF598-mediated eS10 ubiquitination (Juszkiewicz et al. 2020b; Narita et al. 2022; Best et al. 2023), is required to clear collided ribosomes under these conditions. Notably, our findings indicate that the persistence of stalled ribosomes following tRNA synthetase inhibition is not due to an overwhelmed RQC pathway, which has been suggested by the substoichiometric ratios of RQC factors compared with estimated ribosome numbers (Wu et al. 2020) and shown during widespread RNA damage (Stoneley et al. 2022). Instead, our data suggest that, under severe inhibition of tRNA charging, ribosome collisions likely make up a minor subset of the total ribosome stalls.

A prediction from our model is that other stresses that activate the ISR and suppress translation elongation will also inhibit RNP granule assembly. RNA damage (caused by UV stress, methyl methanesulfonate, nitric oxide, or 4-nitroquinoline 1-oxide) and chemotherapeutics (such as etoposide and cisplatin) activate the ISR and cause ribosome stalling (Wu et al. 2020; Yan and Zaher 2021; Stoneley et al. 2022; Ryder et al. 2023; Sinha et al. 2024). Strikingly, these RNA-damaging stresses and chemotherapeutics induce few or no canonical stress granules to form (Arimoto et al. 2008; Aulas et al. 2017, 2018; Ying and Khaperskyy 2020; Wollen et al. 2021; Pietras et al. 2022; Martin et al. 2023). Our study provides an explanation for impaired SG assembly in these contexts and cautions against using SGs as markers of the ISR. We propose that SGs are signal integrators that mark when translation initiation is inhibited and that mRNAs are freed from ribosomes through ongoing elongation or ribosome release.

Our work demonstrates that the RQC machinery is in competition with the ISR in a broader range of contexts than previously recognized (Wu et al. 2020; Yan and Zaher 2021; Nanjaraj Urs et al. 2024). We showed that disomes, which can trigger GCN2 activation (Wu et al. 2020; Pochopien et al. 2021; Yan and Zaher 2021), are detected within 30 min of tRNA synthetase inhibition. Puromycin reduces P-eIF2α levels at early time points, indicating that stalled ribosomes contribute to ISR activation. We considered that puromycin could reduce P-eIF2α levels by binding to GCN2 and competing with uncharged tRNAs; however, GCN2 preferentially binds to uncharged tRNAs (Dong et al. 2000), and puromycin mimics an aminoacylated (tyrosyl) tRNA. Further supporting a role for collided ribosomes in ISR activation, prior work showed that GCN2 phosphorylation is reduced in halofuginone-stressed cells pretreated with cycloheximide, which prevents ribosome collisions (Misra et al. 2024). In addition, we showed that ZNF598-deficient cells exhibit higher P-eIF2α levels than wild-type cells upon halofuginone treatment, consistent with prior findings that the RQC pathway limits ISR activation (Wu et al. 2020; Yan and Zaher 2021; Sinha et al. 2024). Finally, prior work suggests that Gcn2 is preferentially activated by stalled ribosomes with empty A sites (Yan and Zaher 2021), which likely accumulate when tRNA synthetases are inhibited (Misra et al. 2021) or during amino acid deprivation (Wu et al. 2019). Activation of GCN2 serves as a negative feedback loop to repress translation initiation and limit further ribosome stalling that can activate the RSR and RQC pathways (Sinha et al. 2024). These findings underscore the central role of collided ribosomes in coupling translational stress to the ISR.

Emerging evidence suggests that impaired tRNA synthetase activity can be beneficial or detrimental depending on the context. tRNA synthetase inhibitors have therapeutic potential for fibrosis, autoimmunity, systemic sclerosis, cancer, and inflammatory and infectious diseases (Pines and Nagler 1998; Pines et al. 2003; Rock et al. 2007; Vondenhoff and Van Aerschot 2011; Kim et al. 2020a). However, mutations in tRNA synthetases, including loss-of-function *EPRS1* alleles, and other tRNA metabolism genes are associated with peripheral neuropathy and multisystem disorders (Antonellis et al. 2003; Jordanova et al. 2006; Latour et al. 2010; Vester et al. 2013; Tsai et al. 2017; Kuo and Antonellis 2020; Turvey et al. 2022; Jin et al. 2023; Beijer et al. 2024). An outstanding issue is whether and how ISR activation is protective or detrimental in these genetic disease contexts. Animal models expressing mutations in tRNA synthetases or tRNA metabolism genes exhibit markers of the ISR (Blanco et al. 2014; Dogan et al. 2014; Ishimura

et al. 2016; Agnew et al. 2018; Spaulding et al. 2021; Suzuki 2021; Terrey et al. 2021; Zuko et al. 2021; Orellana et al. 2022; Gamage et al. 2025), and fibroblasts from patients with compound heterozygous *EPRS1* mutations hyperactivate the ISR during stress (Jin et al. 2021). Interestingly, ablation of the ISR via *GCN2* knockout can either mitigate or exacerbate disease-associated phenotypes depending on the model system (Ishimura et al. 2016; Spaulding et al. 2021; Terrey et al. 2021). Future studies investigating the coordination of translation initiation, elongation, and RNP granule assembly in disease contexts may suggest therapeutic targets for a wide range of diseases.

A broader implication of our work is that uncollided stalled ribosomes are tolerated within the cell rather than immediately cleared. Tolerance of stalled ribosomes could serve important physiological roles. For example, stalled ribosomes that escape RQC may be critical for mRNA transport in neurons and glial cells to facilitate local translation at distal cellular processes (Barbarese et al. 1995; Kanai et al. 2004; Elvira et al. 2006; Darnell et al. 2011; Müller et al. 2013; Smith et al. 2014; El Fatimy et al. 2016; Langille et al. 2019; Anadolu et al. 2023; Popper et al. 2024). Additionally, pauses in translation elongation enable cotranslational protein folding, translational fidelity, and nascent protein quality control, thereby limiting misfolded, aggregation-prone proteins (Stein and Frydman 2019; Collart and Weiss 2020). During stress, maintaining mRNAs in stalled ribosomes may conserve energy and other resources that would otherwise be required to reinitiate translation (Joazeiro 2017). However, as many tRNA synthetase inhibitors are natural products, ribosome stalling may be toxic in part because animals have not evolved mechanisms to release uncollided ribosomes. Furthermore, activation of the RSR is associated with aging, cell cycle arrest, apoptosis, inflammation, metabolic reprogramming, and other detrimental cellular outcomes (Vind et al. 2020a,b, 2024; Robinson et al. 2022; Snieckute et al. 2022, 2023; Fu et al. 2024; Sinha et al. 2024). Therefore, the selective tolerance of uncollided ribosome stalls may result in a trade-off between preserving cellular functions and risking toxicity from unresolved stalls.

Materials and methods

Cell culture and treatments

U-2 OS cells stably expressing lentivirus transduced EGFP-G3BP1 were described previously (Burke et al. 2020) and kindly shared by James Burke and Roy Parker. Cells were cultured in high-glucose DMEM with glutamine and pyruvate supplemented with 9% FB essence (FBE; Avantor), 2 mM GlutaMAX (Gibco), and 1% penicillin–streptomycin in a 37°C incubator at 5% CO_2. Hoechst staining was done periodically to confirm that cells were free of *Mycoplasma*. The following chemical treatments were performed for the indicated times using 0.2% DMSO or 1% ethanol as carrier controls: 20 or 0.2 µM halofuginone (MedChemExpress [MCE] HY-N1584) in DMSO, 250 µM sodium arsenite (Ricca Chemical Company), 100 µM borrelidin (MCE) in ethanol for 4 h, 40 nM or 1.25 µM thapsigargin (AG Scientific) in DMSO, 2 µM rocaglamide A (MCE), 10 µg/mL puromycin (Gold Biosciences), 0.18 or 180 µM emetine (CalBioChem) in DMSO, 20 µM anisomycin in ethanol, or 5 µg/mL actinomycin D in DMSO. For amino acid deprivation, cells were washed twice with PBS before switching to high-glucose DMEM without arginine or glutamine (US Biological) or supplemented with arginine or glutamine, respectively, for controls and containing 10% dialyzed fetal bovine serum (Gibco) for 1, 4, or 16 h.

To generate *ZNF598* knockout cells, Cas9–sgRNA RNP particles were prepared according to the manufacturer's instructions using a Synthego gene knockout kit for the *ZNF598* gene (sgRNA targets: CGCCTTCCGCACC GAGATCG, GAACCGCCACATCGACCTGC, and GAA CGAGGGTGAGCAGGCAC). EGFP-G3BP1 U-2 OS were nucleofected twice iteratively using a Lonza 4D-nucleofector X unit. Deletions were confirmed using PCR for *ZNF598* genomic DNA (primer sequences: AGTGG TACTCGCGCAAGGACCT and TCCCTTCCCACTGC TCCTGTGG) and Sanger sequencing with alignment to the *ZNF598* genomic DNA (ENSG00000167962) sequence using Benchling (Benchling 2024, Biology Software). Knockout efficiency was estimated using the inference of CRISPR edits (ICE) tool (Synthego performance analysis and ICE analysis 2019, v3.0, Synthego), with 100% indel detection and 94% knockout score determined for the cell pool.

Fluorescence microscopy

To image RNP granules, U-2 OS cells were grown in glass-bottom 96 well plates, treated as indicated, and then fixed for 10 min with 4% paraformaldehyde in PBS. To image stress granules using EGFP-G3BP1, fixed cells were washed once in PBS, incubated in PBS with NucBlue live-cell stain (Hoechst 33342, Invitrogen) for 30 min at room temperature, rinsed with PBS, and then imaged in PBS. Immunofluorescence microscopy was done to image endogenous stress granule markers and P-body markers. After fixation, cells were simultaneously permeabilized and blocked for 10 min at room temperature in AbDil buffer (PBS with 6% BSA, 0.5% Triton X-100). Primary antibody incubations (see Table 1) were performed in 0.5× AbDil in PBS for either 1 h at room temperature or overnight at 4°C. After three washes in PBS for 5 min each, cells were incubated with secondary antibody in 0.5× AbDil with NucBlue for 1 h at room temperature, washed three times for 10 min each, and imaged in PBS.

Simultaneous immunofluorescence and fluorescence in situ hybridization (FISH) were done as described previously (Moon et al. 2020). Briefly, cells were fixed in 4% paraformaldehyde in PBS for 10 min, followed by permeabilization in 0.1% Triton X-100 with 0.2 U/µL RiboLock RNase inhibitor (Thermo Scientific). Cells were then incubated with primary antibodies (Table 1) diluted in PBS with 0.2 U/µL RiboLock for 1 h at room temperature,

Table 1. *Antibodies used in this study*

Antibody target (label)	Manufacturer	Catalog no.	Dilution (method)
Phospho-eIF2α	Abcam	ab32157	1:1000 (Western)
eIF2α	Santa Cruz Biotechnology	SC-133132	1:1000 (Western)
UBAP2L	Cell Signaling Technology	40199	1:200 (immunofluorescence)
PABPC1	Proteintech	66809	1:100 (immunofluorescence)
DCP1A	Santa Cruz Biotechnology	SC-100706	1:100 (immunofluorescence)
EDC4	Proteintech	17737	1:100 (immunofluorescence)
XRN1	Santa Cruz Biotechnology	SC-165985	1:100 (immunofluorescence)
eS10 (also known as RPS10)	Abcam	ab151550	1:500 (Western)
ZNF598	Sigma Aldrich	ZRB1353	1:1000 (Western)
GADD34 (also known as PPP1R15A)	Proteintech	81250	1:1000 (Western)
CReP (also known as PPP1R15B)	Proteintech	83016	1:5000 (Western)
β-Tubulin (DyLight 800)	Thermo Fisher Scientific	16308	1:1000 (Western)
p-p38 (Thr180/Tyr182)	Proteintech	28796	1:1000 (Western)
p-JNK (Thr183/Tyr185)	Proteintech	60666	1:1000 (Western)
Rabbit IgG (Alexa fluor 405)	Invitrogen	A48258	1:1000 (immunofluorescence)
Mouse IgG (Alexa fluor 568)	Invitrogen	A11011	1:1000 (immunofluorescence)
Rabbit IgG (Alexa fluor 647)	Invitrogen	A21244	1:1000 (immunofluorescence)
Rabbit IgG (DyLight 680)	Thermo Fisher Scientific	35568	1:5000 (Western)
Mouse IgG (DyLight 800)	Thermo Fisher Scientific	35521	1:5000 (Western)
Rabbit IgG (peroxidase)	Cell Signaling Technology	7074	1:10,000 (Western)

washed three times for 5 min each with PBS, and then incubated for 45 min at room temperature with fluorescent secondary antibodies (Table 1). Cells were washed three times for 5 min in PBS and fixed in 4% paraformaldehyde in PBS for 10 min. Cells were then incubated in wash buffer A (10% formamide in nuclease-free 2× SSC buffer) for 5 min followed by hybridization buffer (10% dextran sulfate, 10% formamide in 2× SSC) with 30 nt Cy3-labeled oligo(dT) (Integrated DNA Technologies [IDT]) for 20 h at 37°C. Hybridization buffer was removed, and each well was incubated with wash buffer A with NucBlue for 30 min at 37°C, followed by a 30 min wash in wash buffer A. Finally, wash buffer A was replaced with wash buffer B (2× SSC only) before imaging.

Bulk poly(A)$^+$ RNA decay was assessed by treating cells with actinomycin D starting 4 h after adding DMSO (carrier) or 20 µM halofuginone and then fixing cells 1, 2, or 4 h later with 4% paraformaldehyde for 10 min. Cells were washed with PBS and permeabilized with 0.1% Triton X-100 with 0.2 U/µL RiboLock RNase inhibitor (Thermo Scientific). FISH using 30 nt Cy3-oligo(dT) probes was done essentially as above and as described previously (Helton et al. 2025).

Images of fixed cells were collected on an EVOS M5000 fluorescence microscope (Invitrogen) using a 40× objective at room temperature. For live-cell microscopy, media was exchanged to FluoroBrite (Gibco A1896701) supplemented with FBE and GlutaMAX 1 h before treatment. Imaging was performed using Nikon Elements software and the 40× objective of a Nikon Eclipse Ti2 microscope equipped with a Lumencor Spectra III light engine, Andor Life 888 EMCCD camera, and a Tokai Hit stage-top incubator system set to 37°C and 5% CO_2. To assess whether stress granules formed over time upon halofuginone treatment, images were collected every 2 h for 16 h. To determine whether stress granules formed in halofuginone-treated cells in the presence or absence of arsenite or rocaglamide A, images were collected every 30 min for 3 h. The percentage of cells with either stress granules and/or P-bodies was quantified manually using the Cell Counter plugin in ImageJ (Schindelin et al. 2012). PB size and number were determined using the Analyze Particles tool after applying a local normalization filter with the same threshold across images in ImageJ. To determine relative poly(A) RNA levels in cells treated with DMSO or HF and actinomycin D, the intensity of oligo(dT) signal was determined in 10 individual cells (five per frame) in each of $n = 2$ independent replicates using ImageJ. Counts were performed from two frames per condition per independent experimental replicate, with $n = 3$ replicates for every experiment performed except where noted.

Western blotting

Cells were treated as indicated and washed in PBS, and then 1× RIPA buffer with Halt protease, phosphatase inhibitor cocktail (Fisher Scientific), and benzonase (Fisher) were added directly to the plate. Lysates were removed via scraping, supplemented with 4× Laemmli loading buffer and 10× Bolt reducing agent (Fisher), heated for 10 min at 70°C, loaded onto a Bolt 4%–12% Bis-Tris gel (Invitrogen), and electrophoresed in Tris-MES-SDS running buffer

(VWR). Proteins were transferred to a PVDF membrane, and the membrane was stained with total protein Q reagent (Azure Biosystems) and imaged. The membrane was then blocked in TBST buffer with 5% nonfat dry milk for 30 min and incubated with primary antibodies in TBST with milk for 1 h at room temperature or 16–20 h at 4°C. The membrane was washed three times for 5 min each in TBST, followed by 45 min at room temperature with secondary antibodies diluted in TBST buffer with 5% nonfat dry milk. The antibodies used and dilutions are listed in Table 1. The membrane was then washed three times for 10 min each in TBST. All images were collected with an Azure Biosystems c600 imaging system, and band intensities were quantified using the ImageJ gel analysis tool (Schindelin et al. 2012). Relative protein levels were determined by normalizing bands to total protein signal in each lane, and relative levels of phosphorylated eIF2α were normalized to total eIF2α as indicated in each figure.

Polysome and disome profiling

A modified version of the protocol from Ferguson et al. (2023) was used for polysome profiling. Briefly, after treatment, U-2 OS cells were treated with 100 µg/mL cycloheximide for 10 min. Media was aspirated, and cells were washed in ice-cold PBS with 100 µg/mL cycloheximide. Cells were scraped into ice-cold lysis buffer containing 20 mM Tris (pH 7.5), 150 mM NaCl, 5 mM $MgCl_2$, 1% Triton X-100, 1 mM DTT, 1 mg/mL cycloheximide, 80 U/mL RiboLock RNase inhibitor (Thermo Scientific), and 50 U/mL DNase I (Zymo Research). After lysis for 10 min on ice, lysates were centrifuged at 20,000*g* for 30 min at 4°C to remove cell debris, snap-frozen in ethanol–dry ice, and stored at −80°C. For separation of polysomes, lysates were thawed on ice and loaded onto a 10%–50% sucrose gradient in 20 mM Tris (pH 7.5), 150 mM KCl, and 5 mM $MgCl_2$. Gradients were spun at 36,000 rpm for 3 h at 4°C, and polysome profiles were collected using a Biocomp piston gradient fractionator. Absorbance at 260 nm was normalized to 1 for the highest point in each profile. Data were graphed in GraphPad Prism 10.4.0 (GraphPad Software) and exported as .TIF files, and the area under the curve was measured using the ImageJ wand tracing tool (Schindelin et al. 2012). The peaks after the free RNP fraction were defined in order as 40S, 60S, and 80S, and all peaks to the right of the 80S peaks were considered as polysomes.

For disome profiling, nuclease digestion and detection of ribosome collisions were adapted from Ferguson et al. (2023), and the above polysome profiling protocol was modified as follows. Cycloheximide pretreatment was omitted to prevent ribosome stalling artifacts. After thawing, the following were added for every 100 µL of lysate: 7 µL of 300 mM Bis-Tris (pH 6.0), 0.5 µL of 100 mM zinc acetate, and 1 µL (100 U) of nuclease P1 (New England Biolabs). Lysates were incubated for 1 h at 37°C and then separated and measured as above with a reduced centrifugation time of 2.5 h. The highest A260 nm peak was normalized to 1 for each profile, and data were quantified and graphed as above for polysome profiling.

Bioorthogonal noncanonical amino acid tagging

Cells were treated with stressors as indicated and then 10 min prior to collection were switched to methionine-free DMEM with either 4 mM methionine as control (−AHA) or 4 mM azidohomoalanine (AHA) for bioorthogonal noncanonical amino acid tagging (BONCAT). Cells were then lysed in 1× RIPA buffer with Halt protease and phosphatase inhibitor cocktail and benzonase, and the Click-&-Go kit (Vector Laboratories) with Alexa 488 alkyne (Invitrogen) was used for fluorescent labeling of nascent proteins. Laemmli loading buffer (4×) and 10× Bolt reducing agent (Fisher) were added to the samples, which were then heated for 10 min at 70°C, loaded onto a Bolt 4%–12% Bis-Tris gel (Invitrogen), and electrophoresed in Tris-MES-SDS running buffer (VWR). Proteins were transferred to a PVDF membrane, and the clicked fluorophore was imaged on the membrane using an Azure Biosystems c600 imaging system. Total protein staining was then performed with total protein Q reagent (Azure Biosystems). Each lane was quantified with the ImageJ gel analysis tool (Schindelin et al. 2012) and is reported as a ratio of BONCAT signal to total protein signal with the data normalized to the untreated control as 1 for each replicate.

rRNA detection

Cells were incubated with 20 µM halofuginone for 1, 4, or 16 h and then trypsinized and counted, and RNA was extracted from equal cell numbers using the Zymo Quick-RNA minipreparation kit. Equal volumes of RNA were run on a 1% agarose gel with TriTrack dye (Thermo Scientific) and SYBR Safe gel stain (Invitrogen) and imaged (472 excitation and 595 emission) on an Azure Biosystems c600 imaging system.

Quantification and statistics

All experiments were performed for $n = 2$ or 3 independent experimental replicates as indicated, and representative images of a single replicate are shown for each experiment. Data were graphed with bars representing the mean and with error bars indicating the standard error of the mean. Points indicate individual measurements, with matching point colors indicating measurements within a single experimental replicate. Statistical significance was assessed using an ordinary one-way ANOVA followed by Tukey's multiple comparison test or using Student's *t*-test as indicated, and $P \leq 0.05$ indicates significance. Graphs and statistical tests were prepared using GraphPad Prism 10.4.0 (GraphPad Software), SuperPlotsofData (Goedhart 2021), or Python version 3.9.6 using Seaborn version 0.13.1 (https://zenodo.org/records/883859), Pandas version 2.2.0, Numpy version 1.26.3 (Harris et al. 2020), Matplotlib version 3.8.2 (Hunter 2007), and SciPy version 1.12.0 (Virtanen et al. 2020).

Data availability

All data needed to evaluate the conclusions described here are present here and/or in the Supplemental Material. Source data are provided in Supplemental Table S1.

Competing interest statement

The authors declare no competing interests.

Acknowledgments

We thank all members of the Moon laboratory for feedback and helpful discussions. EGFP-G3BP1 U-2 OS cells were generously provided by James Burke and Roy Parker. We thank Anthony Antonellis for helpful discussions and feedback. Figure 8 was created with BioRender.com. This work was supported by National Institutes of Health (NIH) fellowship K12GM111725 (M.B.), NIH fellowship T32GM007544 (N.S.H.), NIH grant R35GM146711 (S.L.M.), and the University of Michigan Center for RNA Biomedicine.

Author contributions: S.L.M. conceived the project. B.D. and S.L.M. designed the study. S.L.M., B.D., and M.B. conceptualized the experiments. M.B., B.D., and S.L.M. curated the data. M.B., B.D., N.S.H., and S.L.M. performed the formal analysis of the data. S.L.M., M.B., and N.S.H. acquired the funding. M.B., B.D., and S.L.M. performed the investigation. M.B., N.S.H., B.D., and S.L.M. performed the methodology. M.B., N.S.H., B.D., and S.L.M. were the project administrators. M.B., N.S.H., B.D., and S.L.M. acquired the resources. N.S.H. was responsible for the software. S.L.M. supervised the study. M.B., N.S.H., B.D., and S.L.M. visualized the data. M.B. and S.L.M. wrote the original draft of the manuscript. M.B., N.S.H., B.D., and S.L.M. reviewed and edited the manuscript.

References

Agnew T, Goldsworthy M, Aguilar C, Morgan A, Simon M, Hilton H, Esapa C, Wu Y, Cater H, Bentley L, et al. 2018. A Wars2 mutant mouse model displays OXPHOS deficiencies and activation of tissue-specific stress response pathways. *Cell Rep* **25:** 3315–3328.e6. doi:10.1016/j.celrep.2018.11.080

Aguilar Rangel M, Stein K, Frydman J. 2024. A machine learning approach uncovers principles and determinants of eukaryotic ribosome pausing. *Sci Adv* **10:** eado0738. doi:10.1126/sciadv.ado0738

Anadolu MN, Sun J, Kailasam S, Chalkiadaki K, Krimbacher K, Li JT-Y, Markova T, Jafarnejad SM, Lefebvre F, Ortega J, et al. 2023. Ribosomes in RNA granules are stalled on mRNA sequences that are consensus sites for FMRP association. *J Neurosci* **43:** 2440–2459. doi:10.1523/JNEUROSCI.1002-22.2023

Antonellis A, Ellsworth RE, Sambuughin N, Puls I, Abel A, Lee-Lin S-Q, Jordanova A, Kremensky I, Christodoulou K, Middleton LT, et al. 2003. Glycyl tRNA synthetase mutations in Charcot-Marie-Tooth disease type 2D and distal spinal muscular atrophy type V. *Am J Hum Genet* **72:** 1293–1299. doi:10.1086/375039

Arimoto K, Fukuda H, Imajoh-Ohmi S, Saito H, Takekawa M. 2008. Formation of stress granules inhibits apoptosis by suppressing stress-responsive MAPK pathways. *Nat Cell Biol* **10:** 1324–1332. doi:10.1038/ncb1791

Aulas A, Fay MM, Lyons SM, Achorn CA, Kedersha N, Anderson P, Ivanov P. 2017. Stress-specific differences in assembly and composition of stress granules and related foci. *J Cell Sci* **130:** 927–937. doi:10.1242/jcs.199240

Aulas A, Lyons SM, Fay MM, Anderson P, Ivanov P. 2018. Nitric oxide triggers the assembly of "type II" stress granules linked to decreased cell viability. *Cell Death Dis* **9:** 1129. doi:10.1038/s41419-018-1173-x

Azzam ME, Algranati ID. 1973. Mechanism of puromycin action: fate of ribosomes after release of nascent protein chains from polysomes. *Proc Natl Acad Sci* **70:** 3866–3869. doi:10.1073/pnas.70.12.3866

Barbarese E, Koppel DE, Deutscher MP, Smith CL, Ainger K, Morgan F, Carson JH. 1995. Protein translation components are colocalized in granules in oligodendrocytes. *J Cell Sci* **108:** 2781–2790. doi:10.1242/jcs.108.8.2781

Baymiller M, Moon S. 2023. Stress granules as causes and consequences of translation suppression. *Antioxid Redox Signal* **39:** 390–409. doi:10.1089/ars.2022.0164

Beijer D, Marte S, Li JC, De Ridder W, Chen JZ, Tadenev ALD, Miers KE, Deconinck T, Macdonell R, Marques W, et al. 2024. Dominant *NARS1* mutations causing axonal Charcot-Marie-Tooth disease expand *NARS1*-associated diseases. *Brain Commun* **6:** fcae070. doi:10.1093/braincomms/fcae070

Bengtson MH, Joazeiro CAP. 2010. Role of a ribosome-associated E3 ubiquitin ligase in protein quality control. *Nature* **467:** 470–473. doi:10.1038/nature09371

Best K, Ikeuchi K, Kater L, Best D, Musial J, Matsuo Y, Berninghausen O, Becker T, Inada T, Beckmann R. 2023. Structural basis for clearing of ribosome collisions by the RQT complex. *Nat Commun* **14:** 921. doi:10.1038/s41467-023-36230-8

Blanco S, Dietmann S, Flores JV, Hussain S, Kutter C, Humphreys P, Lukk M, Lombard P, Treps L, Popis M, et al. 2014. Aberrant methylation of tRNAs links cellular stress to neuro-developmental disorders. *EMBO J* **33:** 2020–2039. doi:10.15252/embj.201489282

Boon NJ, Oliveira RA, Körner P-R, Kochavi A, Mertens S, Malka Y, Voogd R, van der Horst SEM, Huismans MA, Smabers LP, et al. 2024. DNA damage induces p53-independent apoptosis through ribosome stalling. *Science* **384:** 785–792. doi:10.1126/science.adh7950

Brandman O, Stewart-Ornstein J, Wong D, Larson A, Williams CC, Li G-W, Zhou S, King D, Shen PS, Weibezahn J, et al. 2012. A ribosome-bound quality control complex triggers degradation of nascent peptides and signals translation stress. *Cell* **151:** 1042–1054. doi:10.1016/j.cell.2012.10.044

Burke JM, Lester ET, Tauber D, Parker R. 2020. RNase L promotes the formation of unique ribonucleoprotein granules distinct from stress granules. *J Biol Chem* **295:** 1426–1438. doi:10.1074/jbc.RA119.011638

Burke JM, Ratnayake OC, Watkins JM, Perera R, Parker R. 2024. G3BP1-dependent condensation of translationally inactive viral RNAs antagonizes infection. *Sci Adv* **10:** eadk8152. doi:10.1126/sciadv.adk8152

Chandrasekaran V, Juszkiewicz S, Choi J, Puglisi JD, Brown A, Shao S, Ramakrishnan V, Hegde RS. 2019. Mechanism of ribosome stalling during translation of a poly(A) tail. *Nat Struct Mol Biol* **26:** 1132–1140. doi:10.1038/s41594-019-0331-x

Collart MA, Weiss B. 2020. Ribosome pausing, a dangerous necessity for co-translational events. *Nucleic Acids Res* **48:** 1043–1055. doi:10.1093/nar/gkz763

Costa-Mattioli M, Walter P. 2020. The integrated stress response: from mechanism to disease. *Science* **368:** eaat5314. doi:10.1126/science.aat5314

Cougot N, Babajko S, Séraphin B. 2004. Cytoplasmic foci are sites of mRNA decay in human cells. *J Cell Biol* **165:** 31–40. doi:10.1083/jcb.200309008

Darnell JC, Van Driesche SJ, Zhang C, Hung KYS, Mele A, Fraser CE, Stone EF, Chen C, Fak JJ, Chi SW, et al. 2011. FMRP stalls ribosomal translocation on mRNAs linked to synaptic function and autism. *Cell* **146:** 247–261. doi:10.1016/j.cell.2011.06.013

Darnell AM, Subramaniam AR, O'Shea EK. 2018. Translational control through differential ribosome pausing during amino acid limitation in mammalian cells. *Mol Cell* **71:** 229–243.e11. doi:10.1016/j.molcel.2018.06.041

Desroches Altamirano C, Kang M-K, Jordan MA, Borianne T, Dilmen I, Gnädig M, von Appen A, Honigmann A, Franzmann TM, Alberti S. 2024. eIF4F is a thermo-sensing regulatory node in the translational heat shock response. *Mol Cell* **84:** 1727–1741.e12. doi:10.1016/j.molcel.2024.02.038

Dever TE, Feng L, Wek RC, Cigan AM, Donahue TF, Hinnebusch AG. 1992. Phosphorylation of initiation factor 2α by protein kinase GCN2 mediates gene-specific translational control of GCN4 in yeast. *Cell* **68:** 585–596. doi:10.1016/0092-8674(92)90193-G

Dieterich DC, Link AJ, Graumann J, Tirrell DA, Schuman EM. 2006. Selective identification of newly synthesized proteins in mammalian cells using bioorthogonal noncanonical amino acid tagging (BONCAT). *Proc Natl Acad Sci* **103:** 9482–9487. doi:10.1073/pnas.0601637103

Di Fraia D, Marino A, Lee JH, Kelmer Sacramento E, Baumgart M, Bagnoli S, Balla T, Schalk F, Kamrad S, Guan R, et al. 2025. Altered translation elongation contributes to key hallmarks of aging in the killifish brain. *Science* **389:** eadk3079. doi:10.1126/science.adk3079

Di Stefano B, Luo E-C, Haggerty C, Aigner S, Charlton J, Brumbaugh J, Ji F, Rabano Jiménez I, Clowers KJ, Huebner AJ, et al. 2019. The RNA helicase DDX6 controls cellular plasticity by modulating P-body homeostasis. *Cell Stem Cell* **25:** 622–638.e13. doi:10.1016/j.stem.2019.08.018

Dogan SA, Pujol C, Maiti P, Kukat A, Wang S, Hermans S, Senft K, Wibom R, Rugarli EI, Trifunovic A. 2014. Tissue-specific loss of DARS2 activates stress responses independently of respiratory chain deficiency in the heart. *Cell Metab* **19:** 458–469. doi:10.1016/j.cmet.2014.02.004

Doma MK, Parker R. 2006. Endonucleolytic cleavage of eukaryotic mRNAs with stalls in translation elongation. *Nature* **440:** 561–564. doi:10.1038/nature04530

Dong J, Qiu H, Garcia-Barrio M, Anderson J, Hinnebusch AG. 2000. Uncharged tRNA activates GCN2 by displacing the protein kinase moiety from a bipartite tRNA-binding domain. *Mol Cell* **6:** 269–279. doi:10.1016/S1097-2765(00)00028-9

D'Orazio KN, Green R. 2021. Ribosome states signal RNA quality control. *Mol Cell* **81:** 1372–1383. doi:10.1016/j.molcel.2021.02.022

Dubinski A, Gagné M, Peyrard S, Gordon D, Talbot K, Vande Velde C. 2022. Stress granule assembly in vivo is deficient in the CNS of mutant TDP-43 ALS mice. *Hum Mol Genet* **32:** 319–332. doi:10.1093/hmg/ddac206

Eiler DR, Wimberly BT, Bilodeau DY, Taliaferro JM, Reigan P, Rissland OS, Kieft JS. 2024. The *Giardia lamblia* ribosome structure reveals divergence in several biological pathways and the mode of emetine function. *Structure* **32:** 400–410.e4. doi:10.1016/j.str.2023.12.015

El Fatimy R, Davidovic L, Tremblay S, Jaglin X, Dury A, Robert C, De Koninck P, Khandjian EW. 2016. Tracking the fragile X mental retardation protein in a highly ordered neuronal RiboNucleoParticles population: a link between stalled polyribosomes and RNA granules. *PLoS Genet* **12:** e1006192. doi:10.1371/journal.pgen.1006192

Elvira G, Wasiak S, Blandford V, Tong X-K, Serrano A, Fan X, del Rayo Sánchez-Carbente M, Servant F, Bell AW, Boismenu D, et al. 2006. Characterization of an RNA granule from developing brain. *Mol Cell Proteomics* **5:** 635–651. doi:10.1074/mcp.M500255-MCP200

Enam SU, Zinshteyn B, Goldman DH, Cassani M, Livingston NM, Seydoux G, Green R. 2020. Puromycin reactivity does not accurately localize translation at the subcellular level. *eLife* **9:** e60303. doi:10.7554/eLife.60303

Ferguson L, Upton HE, Pimentel SC, Mok A, Lareau LF, Collins K, Ingolia NT. 2023. Streamlined and sensitive mono- and di-ribosome profiling in yeast and human cells. *Nat Methods* **20:** 1704–1715. doi:10.1038/s41592-023-02028-1

Fu Y, Jiang F, Zhang X, Pan Y, Xu R, Liang X, Wu X, Li X, Lin K, Shi R, et al. 2024. Perturbation of METTL1-mediated tRNA N7-methylguanosine modification induces senescence and aging. *Nat Commun* **15:** 5713. doi:10.1038/s41467-024-49796-8

Gamage ST, Khoogar R, Manage SH, DaRos JT, Crawford MC, Georgeson J, Polevoda BV, Sanders C, Lee KA, Nance KD, et al. 2025. Transfer RNA acetylation regulates in vivo mammalian stress signaling. *Sci Adv* **11:** eads2923. doi:10.1126/sciadv.ads2923

Garreau de Loubresse N, Prokhorova I, Holtkamp W, Rodnina MV, Yusupova G, Yusupov M. 2014. Structural basis for the inhibition of the eukaryotic ribosome. *Nature* **513:** 517–522. doi:10.1038/nature13737

Garshott DM, An H, Sundaramoorthy E, Leonard M, Vicary A, Harper JW, Bennett EJ. 2021. iRQC, a surveillance pathway for 40S ribosomal quality control during mRNA translation initiation. *Cell Rep* **36:** 109642. doi:10.1016/j.celrep.2021.109642

Goedhart J. 2021. SuperPlotsOfData—a web app for the transparent display and quantitative comparison of continuous data from different conditions. *Mol Biol Cell* **32:** 470–474. doi:10.1091/mbc.E20-09-0583

Goldman DH, Livingston NM, Movsik J, Wu B, Green R. 2021. Live-cell imaging reveals kinetic determinants of quality control triggered by ribosome stalling. *Mol Cell* **81:** 1830–1840.e8. doi:10.1016/j.molcel.2021.01.029

Grollman AP, Jarkovsky Z. 1975. Emetine and related alkaloids. In *Mechanism of action of antimicrobial and antitumor agents* (ed. Corcoran JW, et al.), pp. 420–435. Springer, Berlin. doi:10.1007/978-3-642-46304-4_27

Guillén-Boixet J, Kopach A, Holehouse AS, Wittmann S, Jahnel M, Schlüßler R, Kim K, Trussina IREA, Wang J, Mateju D, et al. 2020. RNA-induced conformational switching and clustering of G3BP drive stress granule assembly by condensation. *Cell* **181:** 346–361.e17. doi:10.1016/j.cell.2020.03.049

Harding HP, Novoa I, Zhang Y, Zeng H, Wek R, Schapira M, Ron D. 2000. Regulated translation initiation controls stress-induced gene expression in mammalian cells. *Mol Cell* **6:** 1099–1108. doi:10.1016/S1097-2765(00)00108-8

Harding HP, Ordonez A, Allen F, Parts L, Inglis AJ, Williams RL, Ron D. 2019. The ribosomal P-stalk couples amino acid starvation to GCN2 activation in mammalian cells. *eLife* **8:** e50149. doi:10.7554/eLife.50149

Harris CR, Millman KJ, van der Walt SJ, Gommers R, Virtanen P, Cournapeau D, Wieser E, Taylor J, Berg S, Smith NJ, et al.

2020. Array programming with NumPy. *Nature* **585:** 357–362. doi:10.1038/s41586-020-2649-2

Helton NS, Dodd B, Moon SL. 2025. Ribosome association inhibits stress-induced gene mRNA localization to stress granules. *Genes Dev* **39:** 826–848. doi:10.1101/gad.352899.125

Hunter JD. 2007. Matplotlib: a 2D graphics environment. *Comput Sci Eng* **9:** 90–95. doi:10.1109/MCSE.2007.55

Inglis AJ, Masson GR, Shao S, Perisic O, McLaughlin SH, Hegde RS, Williams RL. 2019. Activation of GCN2 by the ribosomal P-stalk. *Proc Natl Acad Sci* **116:** 4946–4954. doi:10.1073/pnas.1813352116

Iordanov MS, Pribnow D, Magun JL, Dinh T-H, Pearson JA, Chen SL-Y, Magun BE. 1997. Ribotoxic stress response: activation of the stress-activated protein kinase JNK1 by inhibitors of the peptidyl transferase reaction and by sequence-specific RNA damage to the α-sarcin/ricin loop in the 28S rRNA. *Mol Cell Biol* **17:** 3373–3381. doi:10.1128/MCB.17.6.3373

Ishimura R, Nagy G, Dotu I, Zhou H, Yang X-L, Schimmel P, Senju S, Nishimura Y, Chuang JH, Ackerman SL. 2014. RNA function. ribosome stalling induced by mutation of a CNS-specific tRNA causes neurodegeneration. *Science* **345:** 455–459. doi:10.1126/science.1249749

Ishimura R, Nagy G, Dotu I, Chuang JH, Ackerman SL. 2016. Activation of GCN2 kinase by ribosome stalling links translation elongation with translation initiation. *eLife* **5:** e14295. doi:10.7554/eLife.14295

Jin D, Wek SA, Kudlapur NT, Cantara WA, Bakhtina M, Wek RC, Musier-Forsyth K. 2021. Disease-associated mutations in a bifunctional aminoacyl-tRNA synthetase gene elicit the integrated stress response. *J Biol Chem* **297:** 101203. doi:10.1016/j.jbc.2021.101203

Jin D, Wek SA, Cordova RA, Wek RC, Lacombe D, Michaud V, Musier-Forsyth K. 2023. Aminoacylation-defective bi-allelic mutations in human EPRS1 associated with psychomotor developmental delay, epilepsy, and deafness. *Clin Genet* **103:** 358–363. doi:10.1111/cge.14269

Joazeiro CAP. 2017. Ribosomal stalling during translation: providing substrates for ribosome-associated protein quality control. *Annu Rev Cell Dev Biol* **33:** 343–368. doi:10.1146/annurev-cellbio-111315-125249

Jordanova A, Irobi J, Thomas FP, Van Dijck P, Meerschaert K, Dewil M, Dierick I, Jacobs A, De Vriendt E, Guergueltcheva V, et al. 2006. Disrupted function and axonal distribution of mutant tyrosyl-tRNA synthetase in dominant intermediate Charcot-Marie-Tooth neuropathy. *Nat Genet* **38:** 197–202. doi:10.1038/ng1727

Juszkiewicz S, Hegde RS. 2017. Initiation of quality control during poly(A) translation requires site-specific ribosome ubiquitination. *Mol Cell* **65:** 743–750.e4. doi:10.1016/j.molcel.2016.11.039

Juszkiewicz S, Chandrasekaran V, Lin Z, Kraatz S, Ramakrishnan V, Hegde RS. 2018. ZNF598 is a quality control sensor of collided ribosomes. *Mol Cell* **72:** 469–481.e7. doi:10.1016/j.molcel.2018.08.037

Juszkiewicz S, Slodkowicz G, Lin Z, Freire-Pritchett P, Peak-Chew S-Y, Hegde RS. 2020a. Ribosome collisions trigger *cis*-acting feedback inhibition of translation initiation. *eLife* **9:** e60038. doi:10.7554/eLife.60038

Juszkiewicz S, Speldewinde SH, Wan L, Svejstrup JQ, Hegde RS. 2020b. The ASC-1 complex disassembles collided ribosomes. *Mol Cell* **79:** 603–614.e8. doi:10.1016/j.molcel.2020.06.006

Kanai Y, Dohmae N, Hirokawa N. 2004. Kinesin transports RNA: isolation and characterization of an RNA-transporting granule. *Neuron* **43:** 513–525. doi:10.1016/j.neuron.2004.07.022

Kedersha N, Cho MR, Li W, Yacono PW, Chen S, Gilks N, Golan DE, Anderson P. 2000. Dynamic shuttling of TIA-1 accompanies the recruitment of mRNA to mammalian stress granules. *J Cell Biol* **151:** 1257–1268. doi:10.1083/jcb.151.6.1257

Kedersha N, Stoecklin G, Ayodele M, Yacono P, Lykke-Andersen J, Fritzler MJ, Scheuner D, Kaufman RJ, Golan DE, Anderson P. 2005. Stress granules and processing bodies are dynamically linked sites of mRNP remodeling. *J Cell Biol* **169:** 871–884. doi:10.1083/jcb.200502088

Kedersha N, Ivanov P, Anderson P. 2013. Stress granules and cell signaling: more than just a passing phase? *Trends Biochem Sci* **38:** 494–506. doi:10.1016/j.tibs.2013.07.004

Keller TL, Zocco D, Sundrud MS, Hendrick M, Edenius M, Yum J, Kim Y-J, Lee H-K, Cortese JF, Wirth DF, et al. 2012. Halofuginone and other febrifugine derivatives inhibit prolyl-tRNA synthetase. *Nat Chem Biol* **8:** 311–317. doi:10.1038/nchembio.790

Khong A, Parker R. 2018. mRNP architecture in translating and stress conditions reveals an ordered pathway of mRNP compaction. *J Cell Biol* **217:** 4124–4140. doi:10.1083/jcb.201806183

Kim S-H, Bae S, Song M. 2020a. Recent development of aminoacyl-tRNA synthetase inhibitors for human diseases: a future perspective. *Biomolecules* **10:** 1625. doi:10.3390/biom10121625

Kim Y, Sundrud MS, Zhou C, Edenius M, Zocco D, Powers K, Zhang M, Mazitschek R, Rao A, Yeo C-Y, et al. 2020b. Aminoacyl-tRNA synthetase inhibition activates a pathway that branches from the canonical amino acid response in mammalian cells. *Proc Natl Acad Sci* **117:** 8900–8911. doi:10.1073/pnas.1913788117

Kuo ME, Antonellis A. 2020. Ubiquitously expressed proteins and restricted phenotypes: exploring cell-specific sensitivities to impaired tRNA charging. *Trends Genet* **36:** 105–117. doi:10.1016/j.tig.2019.11.007

Lageix S, Zhang J, Rothenburg S, Hinnebusch AG. 2015. Interaction between the tRNA-binding and C-terminal domains of yeast Gcn2 regulates kinase activity in vivo. *PLoS Genet* **11:** e1004991. doi:10.1371/journal.pgen.1004991

Langille JJ, Ginzberg K, Sossin WS. 2019. Polysomes identified by live imaging of nascent peptides are stalled in hippocampal and cortical neurites. *Learn Mem* **26:** 351–362. doi:10.1101/lm.049965.119

Latour P, Thauvin-Robinet C, Baudelet-Méry C, Soichot P, Cusin V, Faivre L, Locatelli M-C, Mayençon M, Sarcey A, Broussolle E, et al. 2010. A major determinant for binding and aminoacylation of $tRNA^{Ala}$ in cytoplasmic alanyl-tRNA synthetase is mutated in dominant axonal Charcot-Marie-Tooth disease. *Am J Hum Genet* **86:** 77–82. doi:10.1016/j.ajhg.2009.12.005

Li S, Ikeuchi K, Kato M, Buschauer R, Sugiyama T, Adachi S, Kusano H, Natsume T, Berninghausen O, Matsuo Y, et al. 2022. Sensing of individual stalled 80S ribosomes by Fap1 for nonfunctional rRNA turnover. *Mol Cell* **82:** 3424–3437.e8. doi:10.1016/j.molcel.2022.08.018

Markmiller S, Soltanieh S, Server KL, Mak R, Jin W, Fang MY, Luo E-C, Krach F, Yang D, Sen A, et al. 2018. Context-dependent and disease-specific diversity in protein interactions within stress granules. *Cell* **172:** 590–604.e13. doi:10.1016/j.cell.2017.12.032

Martin JL, Terry SJ, Gale JE, Dawson SJ. 2023. The ototoxic drug cisplatin localises to stress granules altering their dynamics and composition. *J Cell Sci* **136:** jcs260590. doi:10.1242/jcs.260590

Martinez FJ, Pratt GA, Van Nostrand EL, Batra R, Huelga SC, Kapeli K, Freese P, Chun SJ, Ling K, Gelboin-Burkhart C,

et al. 2016. Protein-RNA networks regulated by normal and ALS-associated mutant HNRNPA2B1 in the nervous system. *Neuron* **92:** 780–795. doi:10.1016/j.neuron.2016.09.050

Masson GR. 2019. Towards a model of GCN2 activation. *Biochem Soc Trans* **47:** 1481–1488. doi:10.1042/BST20190331

Mazroui R, Sukarieh R, Bordeleau M-E, Kaufman RJ, Northcote P, Tanaka J, Gallouzi I, Pelletier J. 2006. Inhibition of ribosome recruitment induces stress granule formation independently of eukaryotic initiation factor 2α phosphorylation. *Mol Biol Sci* **17:** 4212–4219. doi:10.1091/mbc.e06-04-0318

Misra J, Holmes MJ, T Mirek E, Langevin M, Kim H-G, Carlson KR, Watford M, Dong XC, Anthony TG, Wek RC. 2021. Discordant regulation of eIF2 kinase GCN2 and mTORC1 during nutrient stress. *Nucleic Acids Res* **49:** 5726–5742. doi:10.1093/nar/gkab362

Misra J, Carlson KR, Spandau DF, Wek RC. 2024. Multiple mechanisms activate GCN2 eIF2 kinase in response to diverse stress conditions. *Nucleic Acids Res* **52:** 1830–1846. doi:10.1093/nar/gkae006

Mollet S, Cougot N, Wilczynska A, Dautry F, Kress M, Bertrand E, Weil D. 2008. Translationally repressed mRNA transiently cycles through stress granules during stress. *Mol Biol Cell* **19:** 4469–4479. doi:10.1091/mbc.e08-05-0499

Moon SL, Morisaki T, Khong A, Lyon K, Parker R, Stasevich TJ. 2019. Multicolour single-molecule tracking of mRNA interactions with RNP granules. *Nat Cell Biol* **21:** 162–168. doi:10.1038/s41556-018-0263-4

Moon SL, Morisaki T, Stasevich TJ, Parker R. 2020. Coupling of translation quality control and mRNA targeting to stress granules. *J Cell Biol* **219:** e202004120. doi:10.1083/jcb.202004120

Müller C, Bauer NM, Schäfer I, White R. 2013. Making myelin basic protein -from mRNA transport to localized translation. *Front Cell Neurosci* **7:** 169. doi:10.3389/fncel.2013.00169

Nanjaraj Urs AN, Lasehinde V, Kim L, McDonald E, Yan LL, Zaher HS. 2024. Inability to rescue stalled ribosomes results in overactivation of the integrated stress response. *J Biol Chem* **300:** 107290. doi:10.1016/j.jbc.2024.107290

Narita M, Denk T, Matsuo Y, Sugiyama T, Kikuguchi C, Ito S, Sato N, Suzuki T, Hashimoto S, Machová I, et al. 2022. A distinct mammalian disome collision interface harbors K63-linked polyubiquitination of uS10 to trigger hRQT-mediated subunit dissociation. *Nat Commun* **13:** 6411. doi:10.1038/s41467-022-34097-9

Orellana EA, Siegal E, Gregory RI. 2022. tRNA dysregulation and disease. *Nat Rev Genet* **23:** 651–664. doi:10.1038/s41576-022-00501-9

Paetz W, Nass G. 1973. Biochemical and immunological characterization of threonyl-tRNA synthetase of two borrelidin-resistant mutants of *Escherichia coli* K12. *Eur J Biochem* **35:** 331–337. doi:10.1111/j.1432-1033.1973.tb02843.x

Pakos-Zebrucka K, Koryga I, Mnich K, Ljujic M, Samali A, Gorman AM. 2016. The integrated stress response. *EMBO Rep* **17:** 1374–1395. doi:10.15252/embr.201642195

Parker R, Sheth U. 2007. P bodies and the control of mRNA translation and degradation. *Mol Cell* **25:** 635–646. doi:10.1016/j.molcel.2007.02.011

Pessina P, Nevo M, Shi J, Kodali S, Casas E, Cui Y, Richards AL, Park EJ, Chen X, Levin-Ferreyra F, et al. 2025. Selective RNA sequestration in biomolecular condensates directs cell fate transitions. *Nat Biotechnol* doi:10.1038/s41587-025-02853-z

Pietras P, Aulas A, Fay MM, Leśniczak-Staszak M, Sowiński M, Lyons SM, Szaflarski W, Ivanov P. 2022. Translation inhibition and suppression of stress granules formation by cisplatin. *Biomed Pharmacother* **145:** 112382. doi:10.1016/j.biopha.2021.112382

Pines M, Nagler A. 1998. Halofuginone: a novel antifibrotic therapy. *Gen Pharmacol* **30:** 445–450. doi:10.1016/S0306-3623(97)00307-8

Pines M, Snyder D, Yarkoni S, Nagler A. 2003. Halofuginone to treat fibrosis in chronic graft-versus-host disease and scleroderma. *Biol Blood Marrow Transplant* **9:** 417–425. doi:10.1016/S1083-8791(03)00151-4

Pitera AP, Szaruga M, Peak-Chew S-Y, Wingett SW, Bertolotti A. 2022. Cellular responses to halofuginone reveal a vulnerability of the GCN2 branch of the integrated stress response. *EMBO J* **41:** e109985. doi:10.15252/embj.2021109985

Pochopien AA, Beckert B, Kasvandik S, Berninghausen O, Beckmann R, Tenson T, Wilson DN. 2021. Structure of Gcn1 bound to stalled and colliding 80S ribosomes. *Proc Natl Acad Sci* **118:** e2022756118. doi:10.1073/pnas.2022756118

Popper B, Bürkle M, Ciccopiedi G, Marchioretto M, Forné I, Imhof A, Straub T, Viero G, Götz M, Schieweck R. 2024. Ribosome inactivation regulates translation elongation in neurons. *J Biol Chem* **300:** 105648. doi:10.1016/j.jbc.2024.105648

Rahmanto AS, Blum CJ, Scalera C, Heidelberger JB, Mesitov M, Horn-Ghetko D, Gräf JF, Mikicic I, Hobrecht R, Orekhova A, et al. 2023. K6-linked ubiquitylation marks formaldehyde-induced RNA–protein crosslinks for resolution. *Mol Cell* **83:** 4272–4289.e10. doi:10.1016/j.molcel.2023.10.011

Riback JA, Katanski CD, Kear-Scott JL, Pilipenko EV, Rojek AE, Sosnick TR, Drummond DA. 2017. Stress-Triggered phase separation is an adaptive, evolutionarily tuned response. *Cell* **168:** 1028–1040.e19. doi:10.1016/j.cell.2017.02.027

Robinson KS, Toh GA, Rozario P, Chua R, Bauernfried S, Sun Z, Firdaus MJ, Bayat S, Nadkarni R, Poh ZS, et al. 2022. ZAKα-driven ribotoxic stress response activates the human NLRP1 inflammasome. *Science* **377:** 328–335. doi:10.1126/science.abl6324

Rock FL, Mao W, Yaremchuk A, Tukalo M, Crépin T, Zhou H, Zhang Y-K, Hernandez V, Akama T, Baker SJ, et al. 2007. An antifungal agent inhibits an aminoacyl-tRNA synthetase by trapping tRNA in the editing site. *Science* **316:** 1759–1761. doi:10.1126/science.1142189

Ryder L, Arendrup FS, Martínez JF, Snieckute G, Pecorari C, Shah RA, Lund AH, Blasius M, Bekker-Jensen S. 2023. Nitric oxide-induced ribosome collision activates ribosomal surveillance mechanisms. *Cell Death Dis* **14:** 467. doi:10.1038/s41419-023-05997-5

Sadlish H, Galicia-Vazquez G, Paris CG, Aust T, Bhullar B, Chang L, Helliwell SB, Hoepfner D, Knapp B, Riedl R, et al. 2013. Evidence for a functionally relevant rocaglamide binding site on the eIF4A–RNA complex. *ACS Chem Biol* **8:** 1519–1527. doi:10.1021/cb400158t

Sanders DW, Kedersha N, Lee DSW, Strom AR, Drake V, Riback JA, Bracha D, Eeftens JM, Iwanicki A, Wang A, et al. 2020. Competing protein–RNA interaction networks control multiphase intracellular organization. *Cell* **181:** 306–324.e28. doi:10.1016/j.cell.2020.03.050

Schindelin J, Arganda-Carreras I, Frise E, Kaynig V, Longair M, Pietzsch T, Preibisch S, Rueden C, Saalfeld S, Schmid B, et al. 2012. Fiji: an open-source platform for biological-image analysis. *Nat Methods* **9:** 676–682. doi:10.1038/nmeth.2019

Shao S, Murray J, Brown A, Taunton J, Ramakrishnan V, Hegde RS. 2016. Decoding mammalian ribosome-mRNA states by translational GTPase complexes. *Cell* **167:** 1229–1240.e15. doi:10.1016/j.cell.2016.10.046

Sheth U, Parker R. 2003. Decapping and decay of messenger RNA occur in cytoplasmic processing bodies. *Science* **300:** 805–808. doi:10.1126/science.1082320

Shoemaker CJ, Eyler DE, Green R. 2010. Dom34:Hbs1 promotes subunit dissociation and peptidyl-tRNA drop-off to initiate no-go decay. *Science* **330:** 369–372. doi:10.1126/science.1192430

Sidhu A, Miller JR, Tripathi A, Garshott DM, Brownell AL, Chiego DJ, Arevang C, Zeng Q, Jackson LC, Bechler SA, et al. 2015. Borrelidin induces the unfolded protein response in oral cancer cells and chop-dependent apoptosis. *ACS Med Chem Lett* **6:** 1122–1127. doi:10.1021/acsmedchemlett.5b00133

Sinha NK, McKenney C, Yeow ZY, Li JJ, Nam KH, Yaron-Barir TM, Johnson JL, Huntsman EM, Cantley LC, Ordureau A, et al. 2024. The ribotoxic stress response drives UV-mediated cell death. *Cell* **187:** 3652–3670.e40. doi:10.1016/j.cell.2024.05.018

Smith R, Rathod RJ, Rajkumar S, Kennedy D. 2014. Nervous translation, do you get the message? A review of mRNPs, mRNA–protein interactions and translational control within cells of the nervous system. *Cell Mol Life Sci* **71:** 3917–3937. doi:10.1007/s00018-014-1660-x

Snieckute G, Genzor AV, Vind AC, Ryder L, Stoneley M, Chamois S, Dreos R, Nordgaard C, Sass F, Blasius M, et al. 2022. Ribosome stalling is a signal for metabolic regulation by the ribotoxic stress response. *Cell Metab* **34:** 2036–2046.e8. doi:10.1016/j.cmet.2022.10.011

Snieckute G, Ryder L, Vind AC, Wu Z, Arendrup FS, Stoneley M, Chamois S, Martinez-Val A, Leleu M, Dreos R, et al. 2023. ROS-induced ribosome impairment underlies ZAKα-mediated metabolic decline in obesity and aging. *Science* **382:** eadf3208. doi:10.1126/science.adf3208

Song M-S, Grabocka E. 2023. Stress granules in cancer. *Rev Physiol Biochem Pharmacol* **185:** 25–52. doi:10.1007/112_2020_37

Spaulding EL, Hines TJ, Bais P, Tadenev ALD, Schneider R, Jewett D, Pattavina B, Pratt SL, Morelli KH, Stum MG, et al. 2021. The integrated stress response contributes to tRNA synthetase-associated peripheral neuropathy. *Science* **373:** 1156–1161. doi:10.1126/science.abb3414

Stein KC, Frydman J. 2019. The stop-and-go traffic regulating protein biogenesis: how translation kinetics controls proteostasis. *J Biol Chem* **294:** 2076–2084. doi:10.1074/jbc.REV118.002814

Stein KC, Morales-Polanco F, van der Lienden J, Rainbolt TK, Frydman J. 2022. Ageing exacerbates ribosome pausing to disrupt cotranslational proteostasis. *Nature* **601:** 637–642. doi:10.1038/s41586-021-04295-4

Stoneley M, Harvey RF, Mulroney TE, Mordue R, Jukes-Jones R, Cain K, Lilley KS, Sawarkar R, Willis AE. 2022. Unresolved stalled ribosome complexes restrict cell-cycle progression after genotoxic stress. *Mol Cell* **82:** 1557–1572.e7. doi:10.1016/j.molcel.2022.01.019

Sundaramoorthy E, Leonard M, Mak R, Liao J, Fulzele A, Bennett EJ. 2017. ZNF598 and RACK1 regulate mammalian ribosome-associated quality control function by mediating regulatory 40S ribosomal ubiquitylation. *Mol Cell* **65:** 751–760.e4. doi:10.1016/j.molcel.2016.12.026

Sundrud MS, Koralov SB, Feuerer M, Calado DP, Kozhaya AE, Rhule-Smith A, Lefebvre RE, Unutmaz D, Mazitschek R, Waldner H, et al. 2009. Halofuginone inhibits T_H17 cell differentiation by activating the amino acid starvation response. *Science* **324:** 1334–1338. doi:10.1126/science.1172638

Suzuki T. 2021. The expanding world of tRNA modifications and their disease relevance. *Nat Rev Mol Cell Biol* **22:** 375–392. doi:10.1038/s41580-021-00342-0

Teixeira D, Sheth U, Valencia-Sanchez MA, Brengues M, Parker R. 2005. Processing bodies require RNA for assembly and contain nontranslating mRNAs. *RNA* **11:** 371–382. doi:10.1261/rna.7258505

Terrey M, Adamson SI, Gibson AL, Deng T, Ishimura R, Chuang JH, Ackerman SL. 2021. GTPBP1 resolves paused ribosomes to maintain neuronal homeostasis. *eLife* **10:** e70785. doi:10.7554/eLife.70785

Tesina P, Lessen LN, Buschauer R, Cheng J, Wu CC-C, Berninghausen O, Buskirk AR, Becker T, Beckmann R, Green R. 2020. Molecular mechanism of translational stalling by inhibitory codon combinations and poly(A) tracts. *EMBO J* **39:** e103365. doi:10.15252/embj.2019103365

Thomas EN, Kim KQ, McHugh EP, Marcinkiewicz T, Zaher HS. 2020. Alkylative damage of mRNA leads to ribosome stalling and rescue by trans translation in bacteria. *eLife* **9:** e61984. doi:10.7554/eLife.61984

Tsai P-C, Soong B-W, Mademan I, Huang Y-H, Liu C-R, Hsiao C-T, Wu H-T, Liu T-T, Liu Y-T, Tseng Y-T, et al. 2017. A recurrent WARS mutation is a novel cause of autosomal dominant distal hereditary motor neuropathy. *Brain* **140:** 1252–1266. doi:10.1093/brain/awx058

Turvey AK, Horvath GA, Cavalcanti ARO. 2022. Aminoacyl-tRNA synthetases in human health and disease. *Front Physiol* **13:** 1029218. doi:10.3389/fphys.2022.1029218

Vester A, Velez-Ruiz G, McLaughlin HM, NISC Comparative Sequencing Program, Lupski JR, Talbot K, Vance JM, Züchner S, Roda RH, Fischbeck KH, et al. 2013. A loss-of-function variant in the human histidyl-tRNA synthetase (*HARS*) gene is neurotoxic in vivo. *Hum Mutat* **34:** 191–199. doi:10.1002/humu.22210

Vind AC, Genzor AV, Bekker-Jensen S. 2020a. Ribosomal stress-surveillance: three pathways is a magic number. *Nucleic Acids Res* **48:** 10648–10661. doi:10.1093/nar/gkaa757

Vind AC, Snieckute G, Blasius M, Tiedje C, Krogh N, Bekker-Jensen DB, Andersen KL, Nordgaard C, Tollenaere MAX, Lund AH, et al. 2020b. ZAKα recognizes stalled ribosomes through partially redundant sensor domains. *Mol Cell* **78:** 700–713.e7. doi:10.1016/j.molcel.2020.03.021

Vind AC, Wu Z, Firdaus MJ, Snieckute G, Toh GA, Jessen M, Martínez JF, Haahr P, Andersen TL, Blasius M, et al. 2024. The ribotoxic stress response drives acute inflammation, cell death, and epidermal thickening in UV-irradiated skin in vivo. *Mol Cell* **84:** 4774–4789.e9. doi:10.1016/j.molcel.2024.10.044

Virtanen P, Gommers R, Oliphant TE, Haberland M, Reddy T, Cournapeau D, Burovski E, Peterson P, Weckesser W, Bright J, et al. 2020. SciPy 1.0: fundamental algorithms for scientific computing in Python. *Nat Methods* **17:** 261–272. doi:10.1038/s41592-019-0686-2

Vondenhoff GHM, Van Aerschot A. 2011. Aminoacyl-tRNA synthetase inhibitors as potential antibiotics. *Eur J Med Chem* **46:** 5227–5236. doi:10.1016/j.ejmech.2011.08.049

Wek RC, Jackson BM, Hinnebusch AG. 1989. Juxtaposition of domains homologous to protein kinases and histidyl-tRNA synthetases in GCN2 protein suggests a mechanism for coupling GCN4 expression to amino acid availability. *Proc Natl Acad Sci* **86:** 4579–4583. doi:10.1073/pnas.86.12.4579

Wek SA, Zhu S, Wek RC. 1995. The histidyl-tRNA synthetase-related sequence in the eIF-2α protein kinase GCN2 interacts with tRNA and is required for activation in response to starvation for different amino acids. *Mol Cell Biol* **15:** 4497–4506. doi:10.1128/MCB.15.8.4497

Wollen KL, Hagen L, Vågbø CB, Rabe R, Iveland TS, Aas PA, Sharma A, Sporsheim B, Erlandsen HO, Palibrk V, et al. 2021. ALKBH3 partner ASCC3 mediates P-body formation and selective clearance of MMS-induced 1-methyladenosine

and 3-methylcytosine from mRNA. *J Transl Med* **19:** 287. doi:10.1186/s12967-021-02948-6

Wong W, Bai X-C, Brown A, Fernandez IS, Hanssen E, Condron M, Tan YH, Baum J, Scheres SHW. 2014. Cryo-EM structure of the *Plasmodium falciparum* 80S ribosome bound to the anti-protozoan drug emetine. *eLife* **3:** e03080. doi:10.7554/eLife.03080

Wu CC-C, Zinshteyn B, Wehner KA, Green R. 2019. High-resolution ribosome profiling defines discrete ribosome elongation states and translational regulation during cellular stress. *Mol Cell* **73:** 959–970.e5. doi:10.1016/j.molcel.2018.12.009

Wu CC-C, Peterson A, Zinshteyn B, Regot S, Green R. 2020. Ribosome collisions trigger general stress responses to regulate cell fate. *Cell* **182:** 404–416.e14. doi:10.1016/j.cell.2020.06.006

Yan LL, Zaher HS. 2021. Ribosome quality control antagonizes the activation of the integrated stress response on colliding ribosomes. *Mol Cell* **81:** 614–628.e4. doi:10.1016/j.molcel.2020.11.033

Yang P, Mathieu C, Kolaitis R-M, Zhang P, Messing J, Yurtsever U, Yang Z, Wu J, Li Y, Pan Q, et al. 2020. G3BP1 is a tunable switch that triggers phase separation to assemble stress granules. *Cell* **181:** 325–345.e28. doi:10.1016/j.cell.2020.03.046

Yin JZ, Keszei AFA, Houliston S, Filandr F, Beenstock J, Daou S, Kitaygorodsky J, Schriemer DC, Mazhab-Jafari MT, Gingras A-C, et al. 2024. The HisRS-like domain of GCN2 is a pseudoenzyme that can bind uncharged tRNA. *Structure* **32:** 795–811.e6. doi:10.1016/j.str.2024.02.021

Ying S, Khaperskyy DA. 2020. UV damage induces G3BP1-dependent stress granule formation that is not driven by mTOR inhibition-mediated translation arrest. *J Cell Sci* **133:** jcs248310. doi:10.1242/jcs.248310

Yip MCJ, Shao S. 2021. Detecting and rescuing stalled ribosomes. *Trends Biochem Sci* **46:** 731–743. doi:10.1016/j.tibs.2021.03.008

You C, Dai X, Wang Y. 2017. Position-dependent effects of regioisomeric methylated adenine and guanine ribonucleosides on translation. *Nucleic Acids Res* **45:** 9059–9067. doi:10.1093/nar/gkx515

Zaborske JM, Narasimhan J, Jiang L, Wek SA, Dittmar KA, Freimoser F, Pan T, Wek RC. 2009. Genome-wide analysis of tRNA charging and activation of the eIF2 kinase Gcn2p. *J Biol Chem* **284:** 25254–25267. doi:10.1074/jbc.M109.000877

Zhao S, Cordes J, Caban KM, Götz MJ, Mackens-Kiani T, Veltri AJ, Sinha NK, Weickert P, Kaya S, Hewitt G, et al. 2023. RNF14-dependent atypical ubiquitylation promotes translation-coupled resolution of RNA-protein crosslinks. *Mol Cell* **83:** 4290–4303.e9. doi:10.1016/j.molcel.2023.10.012

Zuko A, Mallik M, Thompson R, Spaulding EL, Wienand AR, Been M, Tadenev ALD, van Bakel N, Sijlmans C, Santos LA, et al. 2021. tRNA overexpression rescues peripheral neuropathy caused by mutations in tRNA synthetase. *Science* **373:** 1161–1166. doi:10.1126/science.abb3356

tRNA synthetase activity is required for stress granule and P-body assembly

Max Baymiller, Noah S. Helton, Benjamin Dodd, et al.

Genes Dev. published online January 14, 2026
Access the most recent version at doi:10.1101/gad.353535.125